A facility for pion-induced nuclear reaction studies with HADES

EPJ manuscript No.
(will be inserted by the editor)

A Facility For Pion Induced Nuclear Reaction Studies With HADES

(HADES Collaboration)

J. Adamczewski-Musch[4], O. Arnold[9,10], C. Behnke[8], A. Belounnas[15], A. Belyaev[7] ,J.C. Berger-Chen[9,10], J. Biernat[3], A. Blanco[2], C. Blume[8], M. Böhmer[10], P. Bordalo[2], S. Chernenko[7], C. Chlad[16], C. Deveaux[11], J. Dreyer[6], A. Dybczak[3], E. Epple[9,10], L. Fabbietti[9,10], O. Fateev[7], P. Filip[1], P. Fonte[2,19], C. Franco[2], J. Friese[10], I. Fröhlich[8], T. Galatyuk[4,5], J. A. Garzón[17], R. Gernhäuser[10], M. Golubeva[12], F. Guber[12], M. Gumberidze[5,20], S. Harabasz[3,5], T. Heinz[4], T. Hennino[15], S. Hlavac[1], C. Höhne[11], R. Holzmann[4], A. Ierusalimov[7], A. Ivashkin[12], B. Kämpfer[6,21], T. Karavicheva[12], B. Kardan[8], I. Koenig[4], W. Koenig[4], B. W. Kolb[4], G. Korcyl[3], G. Kornakov[5], R. Kotte[6], A. Kugler[16], T. Kunz[10], A. Kurepin[12], A. Kurilkin[7], P. Kurilkin[7], V. Ladygin[7], R. Lalik[9,10], K. Lapidus[9,10], A. Lebedev[13], L. Lopes[2], M. Lorenz[8], T. Mahmoud[11], L. Maier[10], A. Mangiarotti[2], J. Markert[8], S. Maurus[10] V. Metag[11], J. Michel[8], D. M. Mihaylov[9,10], S. Morozov[12,22], C. Müntz[8], R. Münzer[9,10], L. Naumann[6], K. N. Nowakowski[3], M. Palka[3], V. Pechenov[4], O. Pechenova[8], O. Petukhov[12,22], J. Pietraszko[4], W. Przygoda[3], S. Ramos[2], B. Ramstein[15], A. Reshetin[12], P. Rodriguez-Ramos[16], P. Rosier[15], A. Rost[5], A. Sadovsky[12], P. Salabura[3], T. Scheib[8], C. J. Schmidt[4], K. Schmidt-Sommerfeld[10], H. Schuldes[8], E. Schwab[4], A. Scordo[18], F. Scozzi[5,15], F. Seck[5], P. Sellheim[8], J. Siebenson[10], L. Silva[2], Yu.G. Sobolev[16], S. Spataro[23], H. Ströbele[8], J. Stroth[4,8], P. Strzempek[3], C. Sturm[4], O. Svoboda[16], P. Tlusty[16], M. Traxler[4], H. Tsertos[14], E. Usenko[12], V. Wagner[16], C. Wendisch[4], M. G. Wiebusch[8], J. Wirth[9,10], Y. Zanevsky[7], P. Zumbruch[4]

[1] Institute of Physics, Slovak Academy of Sciences, 84228 Bratislava, Slovakia
[2] Laboratório de Instrumentação e Física Experimental de Partículas, 3004-516 Coimbra, Portugal
[3] Smoluchowski Institute of Physics, Jagiellonian University of Cracow, 30-059 Kraków, Poland
[4] GSI Helmholtzzentrum für Schwerionenforschung GmbH, 64291 Darmstadt, Germany
[5] Technische Universität Darmstadt, 64289 Darmstadt, Germany
[6] Institut für Strahlenphysik, Helmholtz-Zentrum Dresden-Rossendorf, 01314 Dresden, Germany
[7] Joint Institute of Nuclear Research, 141980 Dubna, Russia
[8] Institut für Kernphysik, Goethe-Universität, 60438 Frankfurt, Germany
[9] Excellence Cluster 'Origin and Structure of the Universe' , 85748 Garching, Germany
[10] Physik Department E62, Technische Universität München, 85748 Garching, Germany
[11] II.Physikalisches Institut, Justus Liebig Universität Giessen, 35392 Giessen, Germany
[12] Institute for Nuclear Research, Russian Academy of Science, 117312 Moscow, Russia
[13] Institute of Theoretical and Experimental Physics, 117218 Moscow, Russia
[14] Department of Physics, University of Cyprus, 1678 Nicosia, Cyprus
[15] Institut de Physique Nucléaire, CNRS-IN2P3, Univ. Paris-Sud, Université Paris-Saclay, F-91406 Orsay Cedex, France
[16] Nuclear Physics Institute, The Czech Academy of Sciences, 25068 Rez, Czech Republic
[17] LabCAF. F. Física, Univ. de Santiago de Compostela, 15706 Santiago de Compostela, Spain
[18] INFN, Laboratori Nazionali di Frascati, 00044 Fracati (Roma), Italy

[19] also at ISEC Coimbra, Coimbra, Portugal
[20] also at ExtreMe Matter Institute EMMI, 64291 Darmstadt, Germany
[21] also at Technische Universität Dresden, 01062 Dresden, Germany
[22] also at Moscow Engineering Physics Institute (State University), 115409 Moscow, Russia
[23] also at Dipartimento di Fisica and INFN, Università di Torino, 10125 Torino, Italy

Received: date / Revised version: date

Abstract. The combination of a production target for secondary beams, an optimized ion optical beam line setting, in-beam detectors for minimum ionizing particles with high rate capability, and an efficient large acceptance spectrometer around the reaction target constitutes an experimental opportunity to study in detail hadronic interactions utilizing pion beams impinging on nucleons and nuclei. For the 0.4 - 2.0 GeV/c pion momentum regime such a facility is located at the heavy ion synchrotron accelerator SIS18 in Darmstadt (Germany). The layout of the apparatus, performance of its components and encouraging results from a first commissioning run are presented.

PACS. 21.65.Jk Mesons in nuclear matter – 25.80.-e Meson- and hyperon-induced reactions – 29.27.Eg Beam handling; beam transport – 29.30.Aj Charged-particle spectrometers: electric and magnetic – 29.40.Gx Tracking and position-sensitive detectors – 29.85.Ca Data acquisition and sorting

1 Introduction

The availability of secondary pion beams at the GSI accelerator facility [1,2] in Darmstadt, Germany, and the versatile high acceptance dielectron spectrometer HADES [3] provide a world wide unique opportunity to study hadron and dielectron production in pion-nucleon and pion-nucleus interactions. In the range of accessible pion beam momenta - 0.4 GeV/c $\leq$p$_\pi \leq$ 2 GeV/c - inclusive and exclusive measurements of various final states allow to address a broad physics programme (for a recent review see also [4]) including

- Measurements of excitation functions for baryon resonances via 1-pion, 2-pion, and vector meson final states in the center-of-mass energy range $1.4 \leq W \leq 2.1$ GeV.
- Studies of Λ/Σ Hyperon and Kaon production in $\pi^- p$ reactions close to threshold.
- Studies of dielectron, strangeness ($K^\pm$, K^0_S, Λ/Σ), and light vector meson (ρ, ω, Φ) production in pion-nucleus (A) reactions with beam momenta up to p$_\pi$ = 1.7 GeV/c
- Unprecedented studies of dielectron emission in pion-nucleon reactions addressing vector meson-baryon couplings in resonance (R) to virtual photon transitions (R$\rightarrow \gamma^* X$).

This programme has started in 2014 with two pioneering runs studying kaon and ϕ meson production in $\pi^- A$ reactions at pion momenta p$_\pi$ = 1.7 GeV/c and $\pi^- p$ collisions addressing double pion and dielectron production in the second resonance region around $W = 1.52$ GeV.

In this paper, we will summarize the physics motivation and describe details of the pion beam line at GSI with emphasis on the beam optical transport properties (chapter 2) and the installed beam detectors (chapter 3). Results from calibration runs, detector performance studies and first measurements with nuclear targets will be illustrated in chapter 4 and followed by an outlook in chapter 5.

1.1 Excitation Functions of Hadronic Final States in $\pi^- p$ Reactions

The properties of baryonic resonances are deduced from the analysis of photon (real or virtual), pion and proton induced reactions by means of partial wave analysis (PWA). The input to such analyses is provided by various reaction channels, final states and observables [5]. While the photon beam induced data base has recently been enormously enriched thanks to experiments at Mainz/Bonn (Germany) and JLab in the US, the pion reaction data base relies mainly on old and poor statistics measurements [4] and information is in most of the cases not available on the event by event basis needed for modern PWA. Furthermore, pion induced reactions are probing the pion-nucleon vertex directly and may, due to the dominating strong interaction, facilitate the theoretical interpretation of experimental observations.

The two pion production channel is particularly important since it has the largest cross section at these energies, however very little data are available. Data on the final states with light mesons like η, kaon and vector mesons in the exit channel are also needed, in particular for those resonances with small pion-nucleon couplings. Furthermore, the elastic channel needs to be measured with significantly increased statistics in order to provide better constraints for the partial wave analyses. The new facility paves the way for precise scans (with W bins of width $20-30$ MeV) in the range of the second to the third resonance region.

Using pion momenta between 0.6 and 1.9 GeV/c allows to cover center of mass energies between 1.43 and 2.1 GeV. Even multi pion final states like $n\pi^+\pi^-$, $p\pi^-\pi^0$ in $\pi^- p$ reactions with cross sections of $4-10$ μb give count rate estimates of around 100k expected events/hour at available beam intensities of $3-4\times10^5$ π/spill in $\simeq$ 1s spills at three seconds long synchrotron cycles.

The elastic ($\pi^- p \rightarrow \pi^- p$) channel can be produced with even larger statistics and will contribute to the world data set analysis SAID [6]. The large geometrical acceptance and high efficiency for pion detection in HADES results in a typical CM angular range of $40-120^\circ$ and allows for a cross section determination of other reaction channels via a reasonable normalisation to SAID solutions.

The future forward straw tube tracker [7] will even extend this coverage significantly.

1.2 Λ/Σ Hyperon and Kaon Production in $\pi^- p$ Reactions Close to Threshold

Analog to the coupling of the $\pi^- p$ initial state to 1- or 2-pion final states, similar measurements can be carried out for kaon-hyperon ($K^{0,+} - \Lambda/\Sigma^{0,-}$) final states. The cross sections and production rates for these reactions are smaller by about one order of magnitude. Count rates are further reduced by the need for exclusive final state identification. However, the presence of only two particles in the final state requires fewer event statistics to perform differential studies. The following exclusive channels can be measured with HADES:

- $\pi^- p \rightarrow \Sigma^- K^+$ for p$_\pi >$ 1.035 GeV/c (reaction threshold), with all decay particles except the neutron detected ($\Sigma^- \rightarrow n\pi^-$).
- $\pi^- p \rightarrow \Lambda K^0_S$ for p$_\pi >$ 0.896 GeV/c (reaction threshold), with K^0_S or Λ decay detected and kinematically refitted for reaction identification.
- $\pi^- p \rightarrow \Sigma^0 K^0_S$ for p$_\pi >$ 1.031 GeV/c (reaction threshold), with K^0_S decay detected and kinematicaly refitted for reaction identification.

Resonant systems in kaon-hyperon channels have been suggested by theoretical predictions [8–11]. A cusp-like structure has been measured in proton-proton collisions at the Σ threshold [12–14]. Utilizing a pion beam of 1.7 GeV/c ($\sqrt{s} = 2.026$ GeV) such predictions can be tested at 20 MeV

Correspondence to: Juergen.Friese@ph.tum.de, joana.wirth@tum.de

above the $K^*\Lambda$ production threshold. This reaction is particularly interesting since the known resonance around 1.9 GeV could couple strongly to the $K^*\Lambda$ final state and would result in an increased cross section close to threshold [15].

1.3 Vector Meson and Strangeness Production in π^-A Reactions

The study of pion induced vector meson production in nuclei via their e^+e^- decay channel offers unique information on their in-medium properties [16,17], complementary to those from heavy ion collisions. For the ρ/ω mesons, such measurements constitute an extension of previous $p\,A$ studies [18,19] to much lower momenta close to recoilless production [20]. In the particular case of the ϕ meson alternative insights are expected to those obtained from K^+K^- pair decays [21].

The production of strangeness in pion-, proton- and photon- induced reactions has already been pursued to some extent in earlier experiments. The main interest for more detailed investigations of K^0_S, K^+ [22–29] and ϕ [30, 31] production off nuclei is connected to the study of hadron in-medium properties at non-zero baryon densities. Two promising observables are kaon momentum distributions and ϕ or K^- absorption effects in cold nuclear matter. The advantage of pion beam induced reactions is the possible separation of production mechanism and in-medium propagation effects, since the incident pions will be absorbed to a large extent on the surface of the nucleus as predicted by models and verified experimentally by the $A^{2/3}$ dependency of kaon production cross sections [22]. This behaviour is different for photon- and proton-induced reactions in which absorption occurs throughout the whole nuclear volume.

The first approach aims at precise measurements of kaon momentum distributions in π^- or proton induced reactions on carbon and lead nuclei with subsequent comparison to predictions from transport model calculations. The latter ones include a description of reaction dynamics and kaon-nucleus potentials which are predicted to be very different for kaons and anti-kaons [32–35]. Since the radii of heavy nuclei are larger than the average kaon mean free path in nuclear matter ($\lambda \approx 5$ fm), the expected repulsive potential for kaons may manifest itself in a depletion of low momentum components. This is expected to become visible in momentum distribution ratios observed for heavier with respect to lighter target nuclei.

Results obtained in previous experiments show first hints of these effects but suffer from poor event statistics and limited spectrometer acceptances [22,23]. The planned experiments aim at an improved experimental access to the low component of the kaons transverse momentum (p_T) distribution and 1-2 orders of magnitude higher count rate in the region of interest.

For the second approach, production cross section measurements in pion-nucleus reactions will allow detailed absorption studies for ϕ and K^- mesons in cold nuclear matter. Following an idea proposed in ref. [36] the absorption of ϕ mesons in cold nuclear matter has been interpreted as a proof of the widening of the ϕ natural width (from 4 MeV up to 60 MeV) in the medium. Within an eikonal approach, the dependency of the ϕ meson attenuation on mass number A is governed by the imaginary part of the ϕ in-medium self-energy or width. In the low-density approximation [37], this width can be related to an effective ϕN absorption cross section $\sigma_{\phi N}$. However, this approximation is most probably not valid for large baryon densities, where two nucleon effects might be significant. So far, ϕ absorption in different nuclei has not been studied in pion induced reactions. Hence, these measurements should provide valuable complementary information to results obtained with photon and proton beams [38–40].

Furthermore, the study of K^- meson production and absorption will be addressed. Here, the microscopic optical potential used to describe the wealth of existing data points measured for kaonic atoms [41] still lacks a good knowledge of its imaginary part (see also ref. [42,43]). Hence, a similar study to that for the ϕ production can be carried out and may shed light on the role of absorption on 1- and 2- nucleons. In spite of experimental difficulties to separate these two contributions, the comparison of kaon and antikaon yields produced off different nuclei may also address the total absorption rate for antikaons and is an important goal of the pion-induced strangeness production program.

1.4 Dielectron Production in $\pi^- p \to n e^+ e^-$ at $p_{\pi^-} \simeq 0.8$ GeV/c

The study of the exclusive $\pi^- p \to n e^+ e^-$ reaction below the ω threshold offers a unique possibility to measure the coupling of baryonic resonances to off-shell vector mesons [44,45], which is of crucial importance for the understanding of medium effects. These couplings are indeed thought to be at the origin of the in-medium modifications of the vector meson spectral function [46,47].

The understanding of the electromagnetic de excitation of composite particles like baryons involving the emission of an electron-positron pair is also interesting by itself. The important figures of merit are the electromagnetic transition form factors (three for $J = 3/2$ and two for $J = 1/2$ resonances) which depend on the mass of the virtual photon. Since the virtual photons are massive (time-like) the transition $R \to N\gamma^*$ probes the structure of the form factors in the time-like region and therefore provides complementary information to the ones obtained from electro-scattering experiments.

The contribution of baryonic resonances to the $\pi^- p \to n e^+ e^-$ reaction can be described in two ways. In a first approach, a baryonic resonance R decays into a ρ or ω meson which subsequently decays into an e^+e^- pair. In the second approach, a resonance Dalitz decay ($R \to n e^+ e^-$) is considered and the time-like electromagnetic form factors have to be introduced. When using the Vector Dominance Model (VDM) for the form factors, the two approaches are equivalent. However, the validity of the VDM approach to baryonic transitions has never been proven. Moreover, it

is known that the strict application of VDM leads to an overestimation of the $R \to n\gamma$ transitions [48].

Hence, a measurement of these cross sections is of importance. Events from the reaction $\pi^- p \to n e^+ e^-$ can be identified using the missing mass technique. Uncertainties ($\pm 3\%$) on the incident pion beam momenta can be reduced to a subpercent level on an event-by-event basis from beam particle positions measured with in-beam tracking detectors. Angular distributions of the γ^* and the lepton angles w.r.t. the γ^*, measured in its rest frame, are important additional observables to characterise spin and parity of the radiating source [49] and will also be measured with good precision.

1.5 Resume

In summary we find that precise data on all reaction channels mentioned above constitute an important input for the correct modelling of pion-nucleon and pion-nucleus reactions. It is obvious that they are necessary for transport model calculations to describe the contributions of secondary reactions inside the fireball of heavy ion collisions. To accomodate the experimental challenges, a pion transport system with in-beam tracking detectors between the production target and the HADES reaction target has to offer a reasonably large acceptance and good momentum resolution better than $\delta p/p = 1\%$. Such a system has been recently set up and successfully commissioned at GSI, Darmstadt (Germany) with proton and pion beams of various momenta and reaction targets.

2 The GSI Pion Beam Line

2.1 Setup Overview

The GSI accelerator complex with a synchrotron of 18 Tm maximum rigidity delivers protons and ions up to beam energies of 4.5 GeV and 2 AGeV, respectively. A dedicated target station for the production of secondary beams has been built already in the nineties [1] and serves several caves. The HADES experiment is connected via a beam line with a tilted dipole system (D1, D2) such as to elevate the standard beam tube height by 0.5 m up to the central axis of the spectrometer. The beam line is depicted in figure 1. The HADES target point is located about 33.5 m downstream of the production target. Position sensitive beam tracking detectors C1 and C2 are mounted close to the intermediate focal planes between the two dipoles (C1) and between the quadrupoles inside the HADES cave (C2). These quadrupoles (Q7, Q8, Q9 with $l = 1$ m and $l = 0.4$ m) can be adjusted individually in position and are relevant for the focusing conditions at the HADES target point.

The range of achievable pion beam momenta depends on the momentum and nature of the primary beam as well as on the production target and its geometry. In a previous study [1] it was shown that fully stripped ^{12}C or ^{14}N ion beams accelerated at the SIS18 charge space limit ($0.8-1.0\times10^{11}$ ions/spill) and focussed onto a 10 cm thick Be target yields the largest pion current at the HADES target point for a central beam momentum $p_\pi = 1$ GeV/c. The current decreases by a factor 2 for $p \simeq 0.7$ GeV/c and $p \simeq 1.5$ GeV/c, respectively. Higher pion momenta require intense primary proton beams at maximum rigidity.

Due to the production kinematics at these relatively low beam energies, the outgoing pion spectrum is wide in momentum and angle. The ion optical properties and geometrical acceptances of the beam line components define the fraction of pions reaching the HADES target as well as their momentum and angular distributions. For the planned physics programme the beam transport system is designed such as to:

- maximize the pion flux on the liquid hydrogen (LH2) and/or segmented solid target in HADES.
- measure the momentum of each individual pion with in-beam detectors.
- optimize the beam purity at the HADES target point.
- minimize the fraction of pions missing the target areas and the close by T_0 detector.

The last item is of particular importance for the reduction of background reactions in target holder materials and for normalization purposes via beam particle counting in the target T_0 detector.

In the following we present the results of systematic simulation studies aiming at an optimization of the ion optical settings. A method is proposed to reconstruct the relevant pion observables on an event-by-event basis. The sensitivity of the pion flux and momentum reconstruction to a variation of the primary beam position is also studied. Simulation results for electron and muon contamination are given and compared to existing experimental data.

2.2 Simulation Procedure

The optimisation of the beam line optics setup has been carried out in two steps. In a first step, a transport program code [50] was used to tune for given dipole settings the quadrupole strengths as well as Q7-Q9 positions in order to achieve maximum transmission in a broad range of reference momenta. The tuning was done in such a way as to ensure achromaticity and foci in vertical and horizontal directions at the final HADES target point. Respective foci were required at the position of the beam tracking detector between the two dipoles. The resulting first and second order transport coefficients have then been used in Monte Carlo simulations in which individual particles were traced all along the beam line inside the geometrical acceptance of dipoles, quadrupoles and detectors.

In the absence of acceleration devices, five variables are sufficient to describe the coordinates of a particle with momentum p in an x-y plane perpendicular to the optical z-axis of the system for a central momentum p_{ref}. In the usual transport notation these read as:

- $x_1 = x$, the coordinate along the horizontal axis,

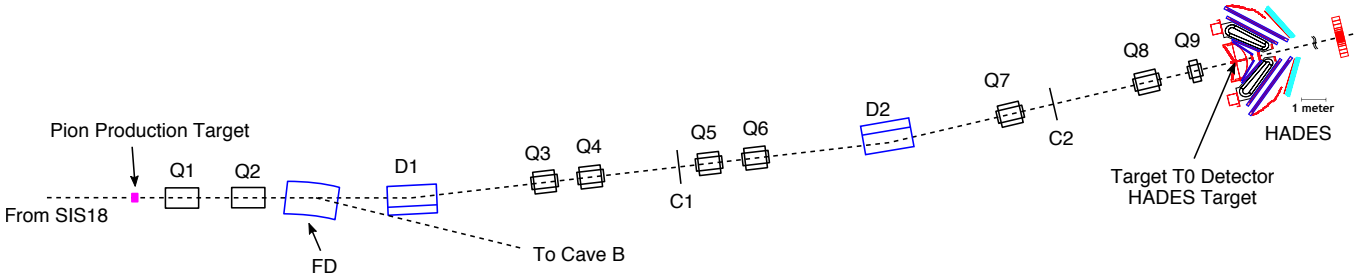

Fig. 1. Schematic overview of the beam line between the pion production target and the HADES cave. The dipole magnets (D), quadrupoles (Q), tracking detectors (C1,C2) and the target T_0 detector are included in the transport simulations. The FD dipole used to direct the beam to cave B is treated as a passive element.

- $x_2 = \theta$, the horizontal angle, defined by $\tan\theta = \mathrm{d}x/\mathrm{d}z = \mathrm{p}_x/\mathrm{p}_z$,
- $x_3 = y$, the coordinate along the vertical axis,
- $x_4 = \varphi$, the vertical angle, defined by $\tan\varphi = \mathrm{d}y/\mathrm{d}z = \mathrm{p}_y/\mathrm{p}_z$,
- $x_6 = \delta$, the momentum offset $\delta = (\mathrm{p} - \mathrm{p}_{ref})/\mathrm{p}_{ref}$.

The standard units used are cm for position variables (x or y), mrad for angles (θ or φ) and % for momentum offset δ.

The coordinates of a particle in any plane perpendicular to the z-axis along the beam line can be written as a function of initial coordinates x_0, θ_0, y_0, φ_0 and δ at the production target using the formula :

$$x_i = \sum_{\substack{j=1,6 \\ j\neq 5}} T_{ij} \cdot x_j + \sum_{\substack{j=1,6 \\ k=j,6 \\ j\neq 5, k\neq 5}} T_{ijk} \cdot x_j \cdot x_k. \qquad (1)$$

The coefficients T_{ij} represent the first order terms, while the second order coefficients T_{ijk} carry the information on the geometrical and chromatic aberrations.

The initial pion distributions at the production target were taken to be Gaussian-like for x_0 and y_0 with a typical rms value of 0.5 mm. Uniform distributions were assumed for θ_0, φ_0, and δ in the ranges $\Delta\theta_0 = \pm 10$ mrad, $\Delta\varphi_0 = \pm 50$ mrad and $\delta = \Delta\mathrm{p}/\mathrm{p} = \pm 6\%$, respectively. This original phase space volume is arbitrarily chosen with limits large enough to contain all particles entering the first quadrupole. The geometrical limitations imposed by the size of the vacuum pipes all along the beam transport line were taken into account by requiring that at each step (entrance and exit face of each element, dipole, quadrupole, drift length, etc.) all off-axis particles stay within the corresponding apertures. The position resolutions of the in-beam detectors as well as multiple scattering effects therein were also included (see paragraph 6.3).

2.3 Flux Optimization

Two scenarios of quadrupole configurations in the spectrometer cave have been studied to obtain a maximum effective pion current at the HADES target point. The first scenario corresponds to the standard HADES beam line configuration for stable ion beams (Q7 – 1 m long, horizontal focusing; Q8 – 1 m long, vertical focusing; Q9 – 0.4 m long, horizontal focusing). Alternatively, the polarities of Q8 and Q9 were exchanged (Q7 – 0.4 m long, horizontal focusing; Q8 – 1 m long, horizontal focusing; Q9 – 1 m long, vertical focusing). The overall geometrical acceptances and hence particle currents are very similar for both cases. However, the standard quadrupole configuration leads to much narrower beam envelopes at the HADES target point. The following simulation results are given for this standard setting.

The two position-sensitive beam tracking detectors give rise to energy loss and multiple scattering. Hence, their positions had to be adjusted properly to optimize acceptance and momentum resolution. The first detector C1 was placed 85.3 cm downstream of the intermediate symmetry plane. In addition it became evident that the detector had to be provided with a proper shielding against secondaries produced by primary beam and projectile fragments hitting the beam pipe and the return yoke of the first dipole. The position of the second detector C2 has been varied between the 7^{th} and the 8^{th} quadrupole to optimize the final pion flux at the HADES target.

The resulting values of the most significant transport coefficients are listed in the appendix in tables 3, 4 and 5. Due to the tilt angle (21.7°) of the dipole system, horizontal and vertical planes are not separated and give rise to non negligible first (T_{14}, T_{32}) and second order ($T_{146}, T_{336}, T_{346}, T_{366}$) coupling terms.

Simulations have been performed for various reference momenta in the range 0.7−1.7 GeV/c. The resulting transmission of remaining pions after each beam line element is shown in figure 2 for the two extreme reference momenta and for some momentum offsets (δ). It should be noted here that losses due to in-flight pion decays have not been taken into account (but see chapter 2.7).

The global transmission for pions of central reference momenta ($\delta = 0\%$) is close to $\simeq 45\%$ and gradually decreases to zero for $|\delta| \geq \pm 6\%$. Pions close to the reference momentum are mainly lost due to the horizontal aperture of the second quadrupole (step 2), the apertures of

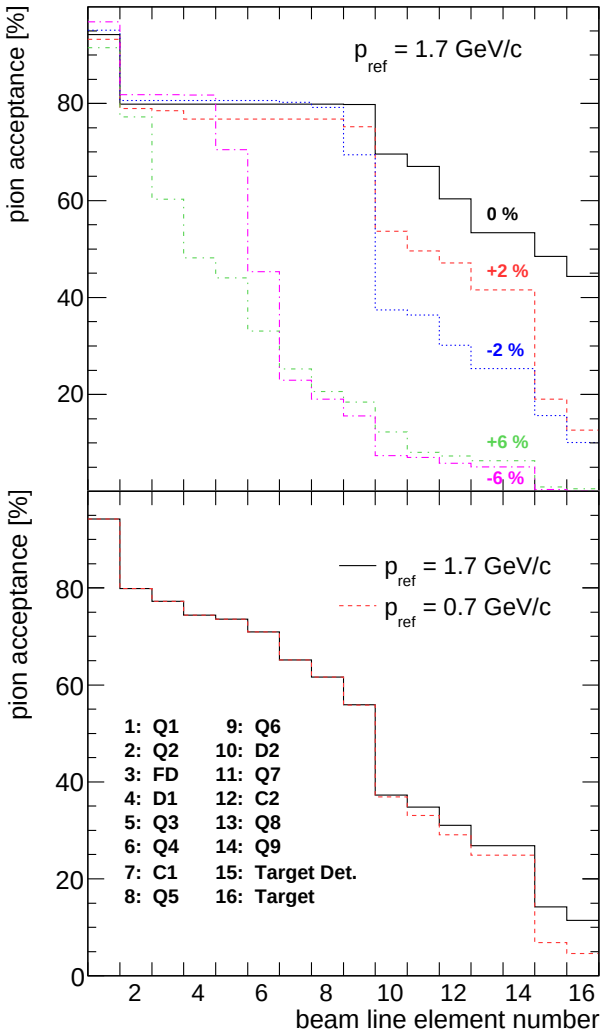

Fig. 2. (Color online) Fraction of pions at the exit of each beam line element. Top: The reference momentum is set to 1.7 GeV/c (black solid line) with respective momentum off-set values as depicted in the figure. Bottom: The initial momentum off-sets are distributed uniformly between -6% and +6% around the reference momentum. The full (dash) histogram corresponds to a reference momentum of 1.7 GeV/c (0.7 GeV/c).

the second dipole, seventh quadrupole, detector C2 (step $10-12$), and finally the reaction target with a diameter of 12 mm (step 16). Losses due to the vertical aperture of the second dipole become much larger for trajectories at $\delta = \pm 2\%$ due to the large dispersion in the vertical direction at this location. The transmission is already reduced by the first quadrupoles due to chromatic aberrations (T_{346}). The different acceptances along the beam line for positive and negative δ values result from the size and sign of the second order coefficients. The overall transmissions integrated over the whole range from -6% to $+6\%$ is shown in the bottom part of figure 2. For a reference momentum of 1.7 GeV/c only a fraction of 11% of all produced pions will hit the interaction target within the

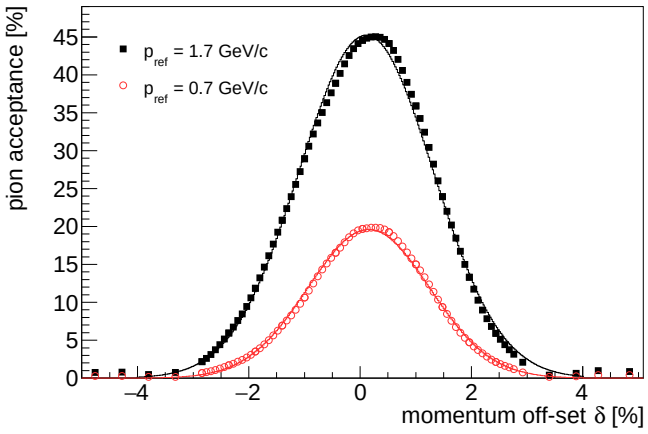

Fig. 3. (Color online) Fraction of pions reaching the HADES target as a function of the offset δ with respect to two reference momenta. The curves correspond to Gaussian fits. The conditions of the simulations are described in the text.

original phase space volume. This fraction is significantly smaller ($\simeq 5\%$) for the lower reference momentum. This rather large difference is due to multiple scattering effects which increase the spatial and angular distributions of the secondary beam. Note that the obtained transmission values depend on the primary beam position, its lateral extension, the initial momentum offset, and the width of the input angular distribution.

The differential transmission distributions are displayed in figure 3 for both reference momenta as a function of the momentum offset. The transmission curves can be approximated by Gaussians centered at offset values $\delta = +0.11\%$ and $\delta = +0.16\%$ with a typical width of $\simeq 1\%(\sigma)$ for $p_{ref} = 0.7$ GeV/c and $p_{ref} = 1.7$ GeV/c, respectively.

2.4 Momentum Reconstruction

The momentum reconstruction of beam pions is of high importance for the analysis of exclusive reaction channels, since it determines to a large extent the achievable missing mass resolution.

In the simulation, the determination of pion momenta is performed utilizing track reconstruction through the measured horizontal and vertical positions X^{C1}, Y^{C1}, X^{C2} and Y^{C2} in the two beam detectors. In a first step, only those terms in Eq. (1) have been kept which lead to a horizontal position shift at the C1 and C2 planes exceeding half the detector pitch (0.078 cm). The transport coefficients of the remaining terms are listed in the appendix in tables 3 and 4.

Nevertheless, the four measured parameters do not allow to unambiguously determine the five unknown pion coordinates at the production target (x_0, θ_0, y_0, φ_0, δ). To solve this problem, the terms coupling to the horizontal position x_0 (e.g. $T_{11}x_0$ and $T_{116}x_0\delta$) are neglected, since they do not contribute much.

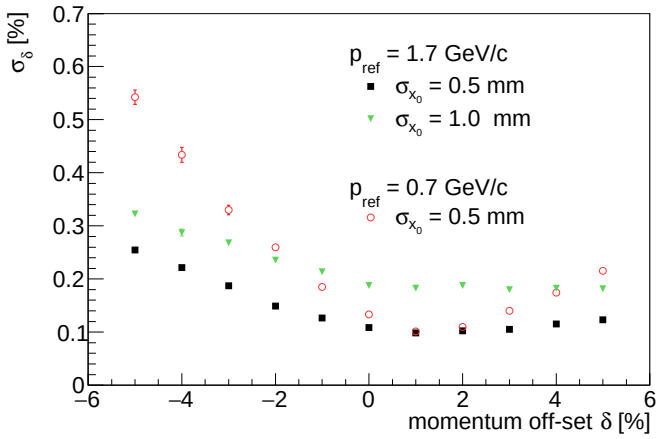

Fig. 4. (Color online) Pion momentum resolution (rms) as a function of the momentum offset δ for different values of reference momenta and primary beam transverse sizes as indicated in the legend.

Due to the significant coupling between the horizontal and vertical positions, the remaining set of four equations have been solved iteratively (see paragraph 6.2 for a detailed explanation of the dedicated algorithm).

Figure 4 shows the achieved resolutions of reconstructed pion momenta for two reference momenta and various momentum offsets δ with initial conditions as defined in paragraph 2.2. The optimum resolution is obtained when the focus is strictly achieved at the detector location, i.e. for $\delta = +1\%$. In this case, the resolution is proportional to the horizontal beam spot size at the production target. The resolution dependence on the momentum offset $|\delta|$ is due to multiple scattering in the upstream detector C1, which affects the momentum determination only for trajectories away from the optical axis and decreases with increasing pion momentum. Inside the range $|\delta| < 3\%$, where the transmission is significant, the resolution stays better than 0.4%, even at the lowest momenta. The asymmetry in resolution degradation for negative δ values is due to the non linear terms involving coupling between δ and θ_0 or φ_0.

2.5 Pion Beam Profiles

For a given primary beam spot position the transport simulations show a few tens of mm broad beam profile centered at the HADES target point, which is mainly due to the size of the transport coefficients T_{12} and T_{34} at the locations of the different elements. The resulting hit patterns at the HADES target point is shown in figure 5.

While most of the pions are focused to distances smaller than 20 mm from the beam axis, the distribution stays wider in the horizontal as compared to the vertical direction.

For solid target foils with 12 mm diameter about 45% and 21% of pions passing the last quadrupole Q9 at 1.7 GeV/c and 0.69 GeV/c, respectively, hit the target. This result is also visible in step 16 of figure 2. The beam halo extends up to ±60 mm in vertical and ±25 mm in horizontal direction, the latter increasing slightly for low momenta.

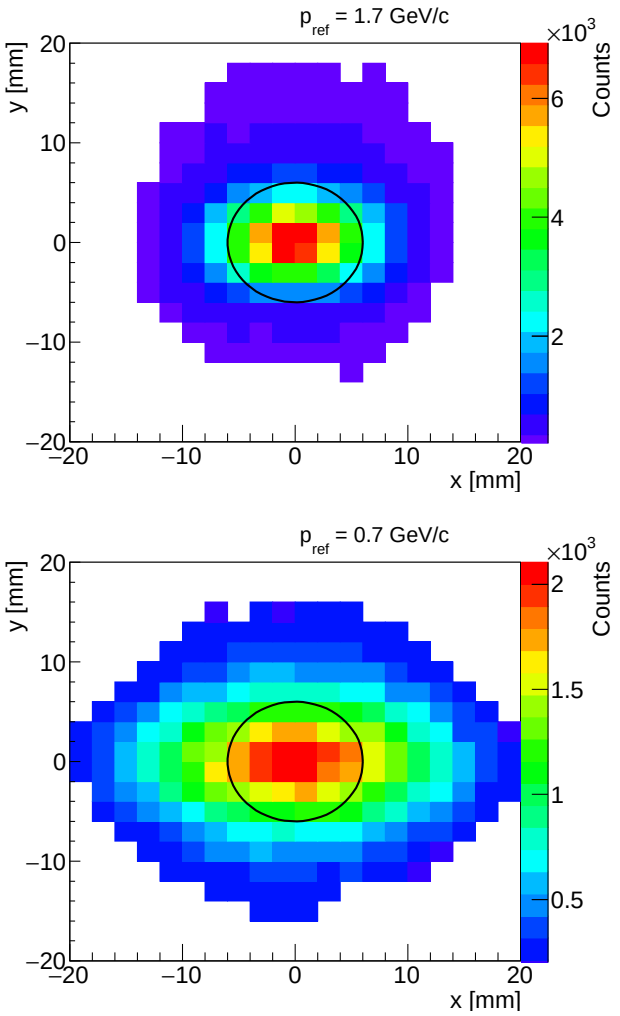

Fig. 5. (Color online) X-Y distributions of pions at the nominal HADES target point for two reference momenta of 1.7 GeV/c (top) and 0.7 GeV/c (bottom). The circle indicates the effective target area. The geometrical acceptance of the beam line is taken into account up to Q9.

At a position 40 cm upstream of the target point, where the 48 mm entrance aperture of the HADES LH2 target is located, about 91% (p = 1.7 GeV/c) to 83% (p = 0.7 GeV/c) of the pions are accepted. This indicates that in experiments with a LH2 target a significant background due to pion interactions in the material of the target holder tube is to be expected. However, the resulting background may be removed by appropriate vertex cuts on tracks measured with the spectrometer.

The determination of the primary beam spot coordinates (θ_0, y_0, φ_0 and δ) itself is performed by track reconstruction with the two beam detectors C1 and C2. The precision of this reconstruction is again mainly affected by multiple scattering in the first beam detector C1. Based on these results, the beam impact coordinates

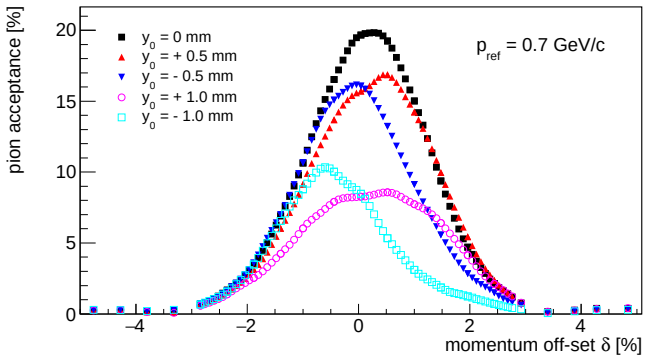

Fig. 6. (Color online) Acceptance curves for primary beam spot shifts in vertical direction. Effects up to $\simeq 50\%$ are possible.

X^H and Y^H at the HADES target can be calculated with the corresponding transport coefficients (see table 5) and compared to the simulation values. The observed resolutions depend on the reference momentum and offset and, for $\delta < 3\,\%$, are in the order of $4-5$ mm and $1-4$ mm (rms) in horizontal and vertical directions perpendicular to the beam axis, respectively.

2.6 Primary Beam Position Effects

A lateral variation of the primary beam spot on the production target has small but visible influences on the transmission and momentum reconstruction. A shift of 1 mm along the horizontal x-direction immediately translates into a global shift of the whole pion momentum spectrum in the order of 0.22%. This is expressed by the linear magnification term $T_{11} = -1.78$ and the dispersion term at the intermediate image $T_{16} = -0.813$ cm/%. However, the transmission to the HADES target point is only weakly affected as long as the shift stays below 2 mm.

A vertical shift shows a completely different and complicated behaviour. First and also second order terms couple the vertical coordinate at the production target to the momentum. For example, while the linear magnification coefficient T_{33} is about -4.0 at the final HADES target point, it is as large as -18.3 at the intermediate image (see appendix table 5). A vertical 0.1 cm shift at the emission point moves pions with reference momentum by 1.8 cm with respect to the center of detector C1, i.e. $\simeq 1/3$ of the detector half width. At the HADES target point, the second order term T_{336} coupling a vertical shift to δ may induce shifts up to 20 mm for $\delta = 3\%$. As a consequence, the yields and momentum transmission curves to the HADES target foil area ($|x| \leq 6$ mm, $|y| \leq 6$ mm) are significantly affected as illustrated in figure 6. The overall losses amount to 10 % to 20 % for a vertical beam shift of 0.5 mm and reach up to 50 % for a 1 mm displacement. In addition, the offset distributions are strongly distorted, too.

Hence, a careful tuning and monitoring of the beam position at the production target is mandatory.

2.7 Beam Purity

In a beam line setting for negative pions, electrons, muons and kaons with same rigidities and emission angles as the pions of interest constitute the dominant contamination of the secondary beam. Lepton induced nuclear interactions will not contribute significantly to the HADES data sample. Nevertheless, their contribution to the detected particle flux in the target T_0 detector may affect normalisation and cross section determinations for the reaction rates of interest.

Electrons with momenta appropriate for the chicane acceptance are mainly created in the decay chain of the copiously produced neutral pions at the production target. These pions decay either in the Dalitz ($\pi^0 \rightarrow \gamma e^+ e^-$ with $BR = 1.17\%$) or via the two photon channel ($\pi^0 \rightarrow \gamma\gamma$ with $BR = 98.8\%$) followed by subsequent pair conversion in the target material. To estimate the expected electron/pion ratio entering the beam line acceptance, a primary fireball production was simulated using the PLUTO [51] event generator for the N+Be reaction at $E_{kin} = 2.0$ AGeV. The inverse slope parameters of transverse mass distributions for charged and neutral pions were taken as input from earlier experimental results observed in C+C collisions at $E_{kin} = 1.0$ AGeV [52]. The photons from π^0 decays were converted into e^+e^- pairs with a probability of 13% corresponding to an average propagation path of 5 cm in Beryllium.

Taking pion decays along the beam line into account, the electron contamination at the HADES target position was found to be 9.6%, 3.2%, and 0.84% for three pion momentum settings ($p_{ref} = 0.7$ GeV/c, 1.0 GeV/c, 1.7 GeV/c), respectively. Most of these electrons stem from photon conversions in the target. These simulated ratios compare well with contamination measurement results reported in Ref. [1] for a similar primary beam, production target and spectrometric beam line setting. In those measurements, electrons and pions were separated via the time of flight method.

Muons stem directly from in-flight leptonic decay of pions ($\pi^- \rightarrow \mu\bar{\nu}_\mu$, BR= 99.99%, $c\tau = 7.8$ m). Hence, the muon contamination at the HADES target position is governed by the pion momentum, decay kinematics and length of the beam line. For the two reference momenta 0.7 GeV/c and 1.7 GeV/c the effective decay lengths are 39.3 m and 95.4 m with decay fractions of 57% and 30%, respectively. The decay kinematics leads to changes in momentum and trajectory angle. Therefore, the acceptance for all muon trajectories has been checked for the beam line downstream of each decay point.

For both pion momentum settings, the simulated μ/π ratio at the HADES target position stays well below 1% (0.65% and 0.75%, respectively). In both cases, the majority of muons reaching the HADES target stem from decays in the drift space after the last quadrupole. Again, the simulation result is in agreement with the experimental findings reported in Ref. [1].

Negative kaons may also be produced through the associate strangeness production reaction $NN \rightarrow NNK^+K^-$, with a kinematical threshold of about 2.5 GeV. In the

given energy regime this process is very strongly suppressed and the kaon momentum distribution is peaked at lower values than for pions. In addition, due to their short effective decay lengths ($c\tau$ = 5.25 m at 0.7 GeV/c and 12.8 m at 1.7 GeV/c), most kaons will decay before reaching the beam tracking detectors and the HADES target. Hence, their influence can be neglected.

Experiments with beams of positive pions suffer from the abundant presence of protons produced at all rigidities. Since related measurements are not foreseen so far, beam purity simulations for positive pion beams have not yet been carried out.

3 Beam Detectors

The beam line to the HADES target point has been equipped with three active beam detectors. Two position sensitive silicon detectors C1 and C2 form the so called CERBEROS system [2] dedicated for track reconstruction of beam particles. A segmented CVD diamond detector is located a few cm upstream of the reaction target and serves for beam counting, time of flight measurements in the spectrometer, and first level trigger purposes. In the following, technical details and obtained performance results are summarized.

3.1 Silicon Tracking Stations

3.1.1 Silicon Sensors

The silicon detectors utilized for CERBEROS are p-type double-sided silicon strip devices mounted on 2.4 mm thick FR4 printed circuit boards (PCB). They have been produced by Micron Semiconductor Ltd.[1] following the TTT-3 model layout designed as the MUSETT silicon array for heavy elements spectroscopy [53]. The choice of p-type sensors (in contrast to the original n-type sensor design) was motivated by the required radiation hardness.

Each single sensor has an active detection area of 10×10 cm^3 and is 300 ± 10 μm thick. Both sides are segmented into 128 parallel strips of length $L = 97.22$ mm with a single strip width of 700 μm and a pitch of $\Delta = 760$ μm. The strips on the rear and front side are oriented perpendicularly to each other. Hence, in a binary read out mode a position measurement resolution of at least $\Delta/\sqrt{12} = 219$ μm can be reached for both directions. The detectors were operated at typical bias voltages between 60 V and 150 V with a DC coupling of each strip to the read out electronics. The guard rings on the sensors had not been connected and were therefore floating.

In addition to the position measurement via binary hit response of strips, a pulse height measurement allows to disentangle single and multi hit events occasionally occurring at large beam intensities and high-multiplicity pulses. In a thin 300 ± 10 μm layer, a considerable fraction of δ electrons knocked out by traversing pions are not reabsorbed in the active volume and lead to a deficit for the measured pion energy loss. This thin layer effect grows with particle momentum [54] and leads to an effective shift of the minimum-ionizing momentum from $450 - 740$ MeV/c. In the foreseen momentum regime between 0.7 GeV/c and 1.7 GeV/c the pions are therefore considered to be minimum ionizing particles with an average energy loss around ΔE $\simeq$ 80 keV. The onset of additional radiation losses at 1.7 GeV/c is still negligible.

Although the energy deposited by a single pion follows a Landau distribution, the single hit amplitudes on both sides of the detector should be similar [2]. Hence, by a pair-wise matching of both amplitudes real hits can be discriminated from random coincidences.

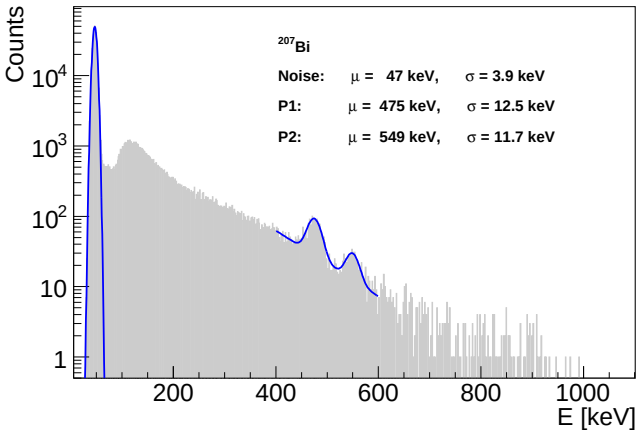

Fig. 7. (Color online) Energy spectrum of a ^{207}Bi source measured with one detector and the n-XYTER frontend. The magenta curves show Gaussian fits combined with exponential tails. The parameters (μ, σ) denote peak position and resolution, respectively.

3.1.2 Energy Resolution

Prior to the installation in the beam line setup the achievable energy resolution of the sensors has been benchmarked in a standalone measurement (see Ref. [55]) with a multichannel nuclear spectroscopy readout. In addition, the detectors have also been connected to the foreseen n-XYTER frontend and readout by an SysCore board [56]. A ^{207}Bi conversion electron source (E = 482, 554, 976, 1045 keV) was used for this calibration. The typical energy spectrum measured with the n-XYTER/SysCore system is depicted in figure 7 and shows two peaks on top of a continuum together with the characteristic noise distribution.

The resulting energy resolutions are in the order of $\simeq 2.5\%$ with a noise contribution corresponding to $1083 - 1120$ e^- for each side of the detector.

[1] **8000 S. Federal Way, P.O. Box 6, Boise, UK**

[2] Pulse height sum of a reconstructed strip cluster

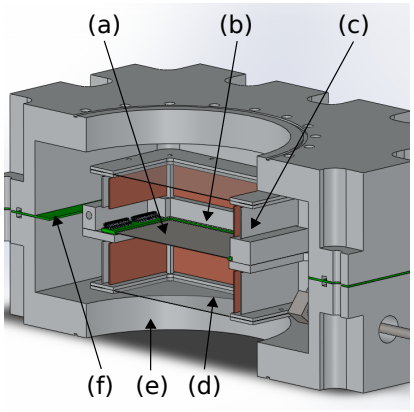

Fig. 8. Schematic cross-section of one tracking station. The silicon detector (a) located in the center is mounted on a copper structure (b,c) with enclosing Mylar foils (d). The ensemble is connected to a carrier PCB (f) sandwiched between the aluminum blocks (e) and providing signal feed-throug lines.

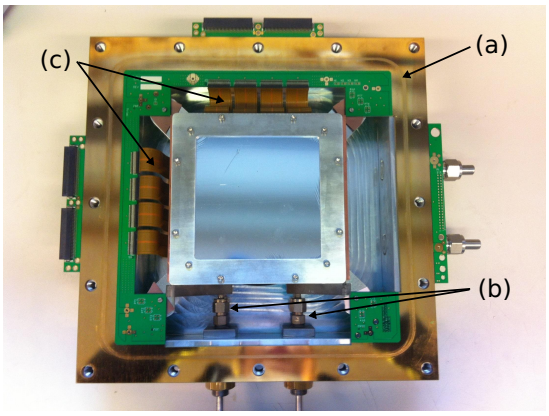

Fig. 9. Top view of the assembled detector with the silicon sensor in the center. The PCB frame (a) with flat Kapton cables (c) to the signal feed throughs is mounted on a copper structure connected to refrigerant tubes (b).

3.1.3 Beam Line Chamber

The two CERBEROS tracking stations are mounted in light tight vacuum chambers at the two positions C1 and C2 along the beam line (see figure 1). Due to the accelerator vacuum requirements a maximum pressure of 10^{-7} mbar has to be maintained at the C1 position, with slightly relaxed conditions at the C2 position. A schematic view of the chamber design is depicted in figure 8. The two halves of each chamber have been machined from aluminum blocks and provide beam tube compatible CF-160 flange connections. The sensor board itself is mounted on a copper block structure enclosed by aluminized Mylar foils on both sides suppressing radiation heating. The whole detector ensemble and a gold plated PCB frame are carried by support pillars. The PCB frame is also sandwiched between the two aluminum seal faces and provides signal line feed-throughs. Signal lines are routed from the detector to the PCB frame via flat Kapton® cables. Additional feed-through lines (maximum 16 LVDS pairs) are foreseen for temperature sensors etc. Sensor cooling is provided by a liquid water-propylenglycole mixture and supplied via dedicated feed-through pipes connected to the copper structure. A photograph of the assembled detector setup is shown in figure 9.

The front-end electronics is mounted close to the PCB signal connectors (left and top edge in figure 9) outside the chamber. Both tracking chambers have been operated continuously at a pressure level of 10^{-7} mbar with a leak rate not exceeding 10^{-9} mbarl/s.

3.1.4 Detector Cooling

Sensor cooling is the standard tool of choice to reduce radiation damage effects on the detector performance and allows for operation in vacuum. This is particularly important for the sensor in tracking station C1 located in the harsh environment close to the production target and exposed to very high secondary particle fluxes. The reverse current at operational bias voltage contributes to electronic noise generation and affects the achievable detector energy resolution.

It has a strong temperature dependence [57]. Particle induced lattice distortions generate additional charge carriers in the sensor bulk material and lead to a signifant increase in the reverse current [58,59] and hence the noise. This degradation can partly be recovered in beam operation breaks (benificial annealing). For longer time scales with high integrated particle doses this short term recovery is overcompensated by the so-called reversal annealing effect [59]. However, this effect is predicted to be completely suppressed at operation temperatures below approximately 0°C [59] such that the reverse current introduced by radiation damage should not increase any longer.

For this reason the silicon sensors have to be cooled down to at least −5°C. Moreover, operation at this temperature level guarantees for a stable performance against thermal runaway in vacuum [60]. Without cooling the missing heat dissipation through convection would lead to a continuous heating up of the sensor. From a detailed investigation of all heat sources in the tracking station a total heat power dissipation of up to 5000 μW has been estimated. The contributions from the various heat sources are listed in table 1.

Table 1. Summary of heat sources and the resulting heating on the detector and cooling system for one tracking station.

Heat source	Heating (Det)	Heating (Cool)
Leakage current	300 μW	
Read-out cables	180-310 μW	
Support pillars		110-210 μW
Heat radiation	200-470 μW	2000-4000 μW
Total	460-860 μW	2110-4210 μW

The layout of the detector cooling system is based on heat transport from the silicon sensor via the carrier FR4

PCB to a heat sink made of copper. A heat conduction pad Kerafoil 86/525 ($\lambda = 5.5$ W/mK, $d = 0.2$ mm) between the PCB and the copper block surfaces improves contact and heat transport. The copper block in turn is flushed with a water-propyleneglycole mixture (60:40) at a temperature of -20°C delivered by a cooling bath thermostat MPC-K6s from Huber [3]. Thermally insulated plastic tubes between the thermostat and the vacuum chamber minimize heat injection from the ambient air to the refrigerant.

In order to reduce the thermal load originating from heat radiation, a metallic screening shield consisting of a frame of aluminum-copper plates ($d = 1.0$ mm, $b = 106.5$ mm, $h = 26.6$ mm/19.7 mm, see figure 8 (c)) and two aluminized Mylar foils ($d = 1.5$ to 2 μm, $w = 252$ μg/cm^2) in front and behind the sensor have been installed. The effect of this shield has been simulated by finite element heat transport calculations, assuming a beam line and chamber surface temperature of $T = 20$°C, a liquid temperature of -12°C, and the emissivity of $\epsilon = 0.57$ for oxidised copper on the inner faces of the frame. The emissivity of polished aluminum ($\epsilon = 0.04$) was taken for the sensor, Mylar foil and outer shielding frame surfaces. The simulations show, that the sensor temperature stays in the range -9 to -2°C for a dissipated power up to 500 mW, while it reaches -7 to 3°C without shield.

The simulation estimates have been verified in measurements with a PT100 sensor mounted on a spare silicon sensor of the same series and installed in a test chamber. The sensor stayed at a temperature -5°C, albeit at a refrigerant temperature of -20°C. During beam operation, the reverse current of the cooled 100 cm^2 large sensor could be reduced by a factor 6 to about 300 nA as compared to operation at room temperature. This value is only slightly above the 200 nA predicted by simulations based on the test bed measurements.

3.1.5 The n-XYTER Read-out Board

The application specific integrated circuit chip (ASIC) n-XYTER v1.1 was employed for individual read-out of the silicon micro-strip channels. This chip was developed within the EU FP6 infrastructure program NMI3, JRA1 with the intention to realize a 128 channel front-end detector read-out ASIC dedicated to the read-out of thermal neutron area sensitive detectors (silicon strip detectors as well as gaseous detectors) in neutron scattering instruments [61]. Unlike typical high energy physics experiments, the statistically incoming neutron signal events are simple in structure, a mere click in the detector. There is no criterion for the pre-selection of events while the distribution of events reveals the physics contents sought. For this reason the n-XYTER was designed as a multi-channel front-end chip realizing freely streaming, self-triggered data read-out. Every channel is equipped with its own discriminator circuit which triggers the registration of a time-stamp and pulse height. The information is stored in a de-randomizing four-level deep fifo on the per channel level from where it is read-out through a token ring scheme. The token ring serves to allocate and focus read-out bandwidth to channels where needed while impeding potentially noisy channels from clogging up the read-out. With this architecture the chip is perfectly suited for the read-out of modern nuclear physics detector systems such as envisioned for FAIR experiments relying upon triggerless, freely streaming data to be analyzed in an external computer farm.

A charge sensitive preamplifier, constructed around a folded cascade circuit forms the input stage. For its superior noise performance an NMOS input transistor has been chosen. Unlike conventional read-out chips, the signal path is split into two shaper branches after the preamplifier as depicted in figure 10. A fast CR-RC shaper drives the timing-critical path including the discriminator with a peaking time of 18 ns at a noise level of less than 1000 ENC at 30pF input capacitance. Upon an incoming signal and discriminator response a 14bit time stamp is latched with a binning resolution of 1ns. The trigger signal further serves to reset a peak detector circuit allocated in the second, slow shaper branch. This slow CR-(RC)2 shaper drives the more noise-critical measurement of the deposited energy, realizing a peaking time of 140 ns. Whereas the fast shaper branch accepts signals of either polarity, merely depending upon the configuration of the discriminator, the slow shaper branch allows to choose polarity inversion in a second stage so that either polarity input signals may be fed to the unipolar peak detector circuit. With the difference in peaking time of the two shaper branches, the discriminator in the fast line resets the peak detector in the slow line in time so that the full peak height will be registered. The signal peak value determined through the peak detector is stored in a corresponding analogue fifo for read-out through the token ring. Event time stamps together with the corresponding analogue peak heights are successively read-out at 32 MHz to an operating FPGA. The particular channel is chosen by means of a token that is asynchronously handed from one channel to the next while channel fifos are unoccupied and sticks to a channel containing data. Upon read-out, the token is released again to mark the next channel in row that contains data which is successively read-out during the next clock cycle. With an overall dynamic range of about 20 fC the n-XYTER may be employed for the detection of minimally ionizing particles (MIPs) with double sided silicon strip detectors as well as for modern micro patterned gaseous detectors (MPGD).

The n-XYTER-chip was mounted on a dedicated front end board (FEB) (see figure 11) placed close to the detector chamber. The sensor signal lines were AC coupled to the chip inputs via an 1 MΩ resistor 10 pF capacitor band pass. With the ohmic sensor side connected to ground, the junction side was supplied with the typical $U = +150$ V operational voltage at an average reverse current below 500 nA (see above). In addition, an external ADC (Analog Devices AD9228) is foreseen for the amplitude measurement.

[3] **Huber Kaeltemaschinenbau AG, D-77656 Offenburg**

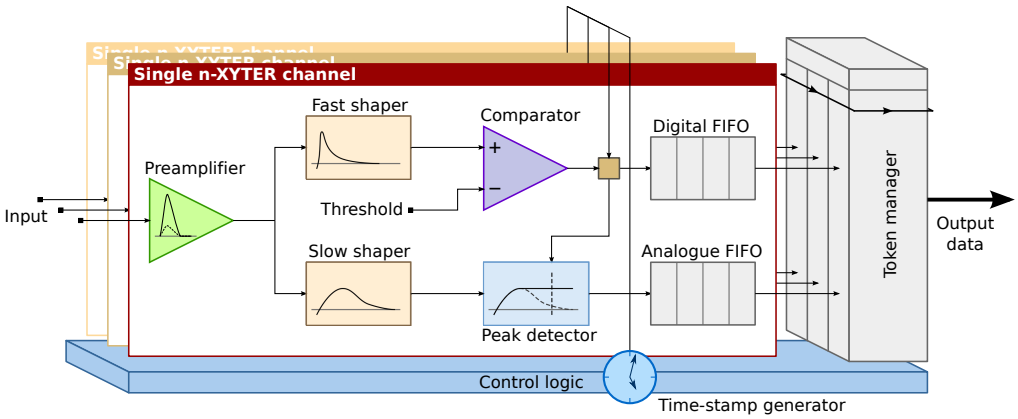

Fig. 10. Block diagram of the n-XYTER architecture. The front end part is individual for each channel. The back-end part joins all channels (token ring architecture) and streams data to a single output bus. The DAC and time-stamp generator deliver common biasing and a time reference for all channels.

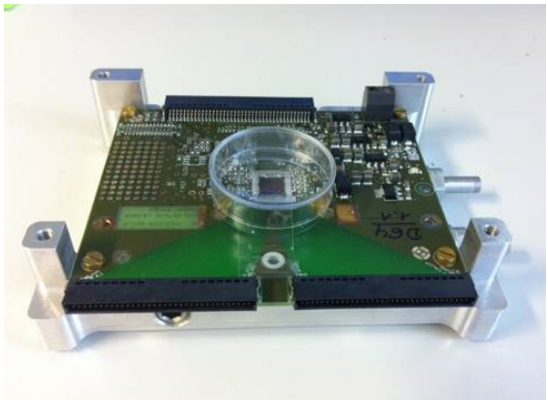

Fig. 11. The n-XYTER read-out board (FEB) mounted on a peltier element cooling block.

Heat dissipation was supported by an aluminum block cooled by a peltier element and forced air ventilation. Dedicated temperature sensors on the FEB allowed to monitor the varying ambient conditions at the beam line installation sites. In this way, also the effective chip temperature and the related base line level of analogue outputs could be determined on a spill by spill basis.

3.1.6 Data Acquisition

The front-end board (FEB) hardware is integrated in the common HADES data acquisition (DAQ) system, in which the read-out of all subsystems is synchronized by reference time signals from a central trigger system (CTS) while data transport is accomplished by a dedicated network protocol (TrbNet) [62].

The connection is provided by a triggered read-out board TRB3 [63] (see figure 12) module based on a general purpose field programmable gate array (FPGA) platform employed for read-out of various HADES subdetectors. The TRB3 board consists of four independent FPGAs (Lattice ECP3) that provide resources to accommodate read-out of any type of detector system such as the in-FPGA TDCs with a timing precision $\simeq$ 15 ps (RMS) or digital logic to the collect data from silicon pixel sensors. A fifth FPGA operates all communication such as a Gigabit Ethernet link to send collected data to a server and an optical link for the DAQ network.

In this application, the TRB3 provides all required functionality to operate the silicon tracker system, consisting of various items beside collecting and recording data from the front-end. As timing and amplitude information is transmitted by different means, a synchronisation between the data received from the ADC and the timing information has to be carried out. As HADES uses a triggered DAQ, not all data is forwarded to storage. Only hits recorded within a defined time window of typically 400 ns around the trigger signal are of interest. To reduce the necessary bandwidth, this filtering is part of the front-end logic. To further reduce the amount of data, no absolute time stamps are transported. The FPGA calculates the relative time of each hit with respect to the trigger signal. This enables the system to encode all hit information in a concise 32 Bit word.

In the realm of controls, a configuration interface (SPI, I2C) needs to be provided to load parameters to both the ASIC and the ADC. Hit information from the n-XYTER ASIC can be used to provide a fast differential signal to the CTS which in turn can issue triggers for the full DAQ system [4].

Like all HADES subsystems, the paradigm of having access to all kind of monitoring information collected directly in the front-ends is followed closely. This means that basic status information of all components as well as statistics on hit rates and ADC measurements are provided by the FPGA firmware. The data can be requested via software and is transported along with trigger information and data over the optical data acquisition network on

[4] A feature that proved useful during commissioning of the silicon tracker while no start detector was installed.

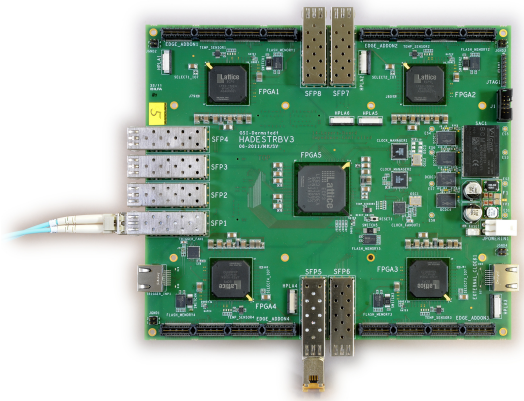

Fig. 12. The TRB3 card. One central FPGA and four I/O FPGAs provide a flexible read-out system.

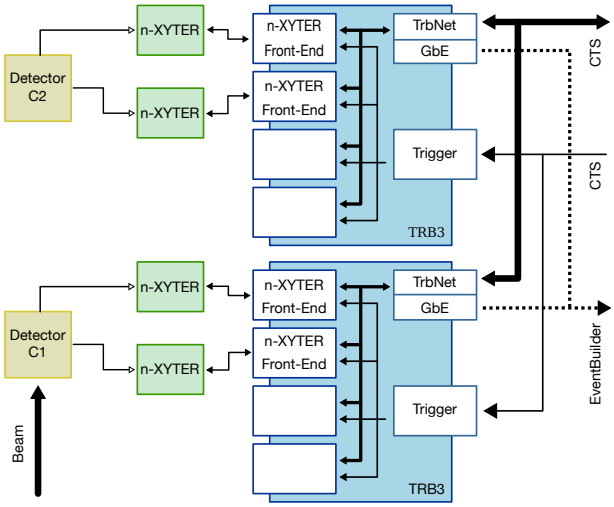

Fig. 13. The TRB3 read-out scheme for the CERBEROS tracking system.

a low-priority channel. This allows to show various status displays in real-time without delays for the more complex analysis of data sent to the server farm.

Each of the two detector stations is equipped with two n-XYTER modules, one for each side of the strip detector. Even though each of the FPGA on the TRB3 could handle the read-out of both of them, this was not implemented for the sake of simplicity. Hence, each of the two stations was served by one TRB3 having one FPGA connected to each of the n-XYTER, one (central) FPGA for communications and two remaining idle (figure 13). The whole setup can be operated within the complete HADES DAQ system as well as a stand-alone setup where no external connections beside power and Ethernet are required. This is accomplished by merely changing the configuration of the central FPGA of the TRB3 to provide the same functionality like the HADES CTS.

The peripheral FPGA is loaded with the n-XYTER operation firmware fulfilling the following tasks:

– data read-out of the n-XYTER,
– I^2C and SPI interfaces for the FEB operation,
– trigger and event building logic,
– TrbNet implementation.

All FEB data are marked with a global time stamp and stored in an internal buffer implemented in the peripheral FPGA. To select only hits belonging to studied physical events in the HADES spectrometer, an event window defined by a window offset and width is set. Only hits within this window (400 ns) are selected by the trigger logic on the board and sent to the Event-Builder. Each hit contains the relative time stamp, channel number, ADC and status flag.

3.1.7 Read-out Performance

The total read-out bandwidth of a TRB3 is 90 Mbyte/s raw data, limited by the throughput of Gigabit Ethernet. This translates to a hit rate of up to 22 MHz summed over all channels and does not constitute a bottleneck in this application even though each n-XYTER front-end can deliver hit data at up to 32 MHz. The anticipated hit rates on the first station of the tracking system are at about 10 MHz, well distributed over the whole detector surface. Hence, the individual channel buffers of the n-XYTER ASIC are unlikely to experience an overflow as long as the single channel hit rate of 2 MHz and/or total bandwidth of the chip are not exceeded. Additionally, the trigger rate of the whole detector setup is in the order of several ten kHz. Combined with the set trigger window of 400 ns, a substantial reduction in data rate by more than 90% is achieved. In total, only about 10 Mbyte/s need to be transported per detector side.

Applying trigger windows and processing of data, as described above, is done at a rate of 100 MHz and does not introduce any additional dead-time larger than the latency of the exchange of trigger information on the DAQ network and the even larger intrinsic dead time of other HADES subsystems. Assuming a typical occupancy of less than 20 channels firing per event, the system is able to take data at a trigger rate of up to 200 kHz, well above the actual rates during the pion beam data taking.

3.2 Target T_0 Detector

In all HADES experiment campaigns a target T_0 detector is used to allow for beam profile optimization and generation of a fast timing signal for trigger purposes and time of flight particle identification. The location of the detector very close to the target is mandatory to minimize beam interactions and resulting charged particle hit loads on the sensitive RICH photo electron detector. In particular for pion beam experiments this device has to fulfill the following requirements:

1. Good timing precision $\delta t \leq 100$ ps for particle identification via time-of-flight.
2. Operation stability for particle fluxes $J \geq 10{\times}10^6 \mathrm{cm}^{-2}\mathrm{s}^{-1}$
3. Detection efficiency for MIPS $\epsilon \simeq 100\%$.

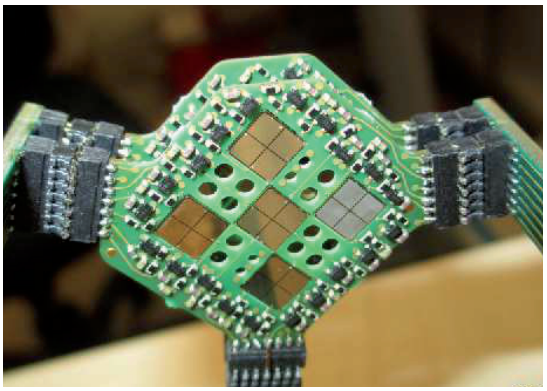

Fig. 14. Photograph of the T_0 detector. Nine metallized sc-CVD diamond sensor plates with fourfold segmented read-out electrodes are mounted on 2 attached PCBs arranged such as to build a 3x3 matrix structure. Read-out, LV and HV supply are mounted on 3 holding PCB rods.

4. Low material budget.
5. Reasonable position resolution of $\delta x < 1$ mm for tracking support and vertex reconstruction.
6. Vacuum operation.
7. Active area $A = 1$ cm^2.

Detectors based on mono-crystalline diamond material produced with the Chemical Vapor Deposition (CVD) process can match the above criteria. This has been demonstrated in tests with prototype devices bombarded with 2.95 GeV proton beams from the COSY facility in FZ Juelich [64]. Such detectors have also been successfully used in earlier HADES campaigns with heavy ion beams.

3.2.1 Detector Design

The target T_0 detector consists of a nine element diamond sensor array arranged on two support boards with 5 and 4 sensors. The device is depicted in figure 14. A diamond crystal thickness of 300 μm has been chosen as a compromise between multiple scattering and a required signal-to-noise ratio $SNR \simeq 40$ at nanosecond rise times. The sensors are operated at typical field strengths $E_{bias} \simeq 0.6\,V/\mu m$. The active area of a single diamond plate is $A = 4.3{\times}4.3$ mm^2 and segmented into 4 quadrants by appropriate front side metallisation. The four-fold segmentation of each diamond sensor allows for a reasonable position resolution and ensures low detector capacitance with correspondingly reduced noise contributions.

An individual sensor quadrant read-out is performed by preamplifiers based on high gain, very low noise SiGe:C RF-transistors mounted onboard close to the detector pads. The 36 preamplified signals are read out via copper lines embedded into the support rods (see figure 14) and guided to vacuum feedthroughs. An external booster/shaper module provides further signal amplification and pulse shaping. Threshold setting and signal discrimination is obtained utilizing the NINO amplifier/discriminator chip with 8 channels ([65]) connected to a standard TRB3 board

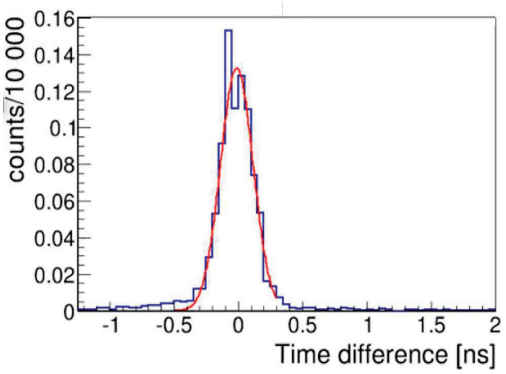

Fig. 15. Two detector timing distribution for correlated signals from protons at 2.95 GeV. The timing precision of individual sensors is $\delta t = 127$ ps$/\sqrt{2} = 91$ ps.

(see above) and successfully operated in previous HADES experiments ([66]).

3.2.2 Performance

The performance achieved with a stack of two prototype detectors in a commissioning proton beam measurement [64] can be summarized as follows:

1. Bias voltage $U_{bias} = 200$ V.
2. Rise time (10% − 90%: 1.35 ns,
3. Signal/RMS noise ratio: 30:1,
4. Expected timing precision: < 100 ps,
5. Preamplifier power consumption: 1.65 mW/channel, in total: 60 mW,
6. Horizontal and vertical pixel resolution (σ): 0.7 mm each.

A sample time distribution of correlated signals in two subsequent detector layers is shown in figure 15. The obtained values agree well with expectations based on detector simulations.

4 Commissioning Experiments

The first experimental campaign with the new ion optical settings and beam detectors was divided into three parts. After a calibration run with primary proton beams for momentum reconstruction two pion beam runs with different incident momentum ranges and reaction targets were carried out. The first of these focussed on pion-nucleus reactions ($\pi^- + A$, $A = W$ or $A = C$) at a central beam momentum of $p^{\pi^-}_{ref} = 1.7$ GeV/c. The second pion run was devoted to reactions ($\pi^- + p$) employing a polyethylene target (C_2H_4) and varying reference momenta in the range 656 Mev/c $\leq p^{\pi^-}_{ref} \leq$ 800 MeV/c. Additional measurements on a pure carbon target served here to determine the background from nuclear reactions.

In both runs primary ^{14}N ion beams at $E_{kin} = 2$ AGeV have been focussed onto the 10 cm thick beryllium production target with intensities of $\approx 10^{10}$ ions/spill. Typical

Table 2. Collected event numbers for various reference momenta in the first pion beam campaign.

Target	$p^{\pi^-}_{ref}$[GeV/c]	Events
Polyethylene (PE)	0.656	42.4M
Polyethylene (PE)	0.690	774.7M
Polyethylene (PE)	0.748	76.5M
Polyethylene (PE)	0.800	52.4M
Carbon (C)	0.656	41.9M
Carbon (C)	0.690	115.7M
Carbon (C)	0.748	42.2M
Carbon (C)	0.800	41.2M
Carbon (C)	1.700	102.6M
Tungsten (W)	1.700	128.5M

pion beam intensities on the HADES reaction target inside the accepted momentum range amounted to $\simeq 200-500$ k per 1-2 seconds long spill. The secondary pion beam spot width at the target focal point was measured with the target T_0 detector to $\delta x \simeq 1$ cm (rms), as expected from the simulations. The recorded event rates were determined by the first level (LVL1) trigger condition requiring a T_0 signal in the target detector and at least two hits on the multiplicity and electron trigger array (META) wall of the HADES detector. However, the obtained timing precision of $\delta t \simeq 250$ ps (σ) did not yet match the expectations, due to extensive pick-up noise (up to 7 mV) in the T_0 detector read-out chain. Nevertheless, a considerable amount of off-vertex reactions could be suppressed already on the trigger level and reduced the recorded data volume significantly.

Timing signals from the CERBEROS beam tracking detector layers (resolution $\sigma = 8.0$ ns) coincident within a 400 ns broad time window with respect to the T_0 signal were used to suppress pile-up and multi hit events in the tracking stations on the LVL1 trigger level. The pulse height information measured in the second station C2 allowed for a correlation of front- and rear-side sensor signals and helped further in background hit suppression.

The collected event statistics with valid LVL1 trigger signals for both runs is listed in table 2.

4.1 Tracking Efficiency

In the proton run, the overall tracking efficiency was estimated to be $\simeq 95\%$. In the pion beam runs the first tracking station (C1) close to the pion production target experienced an average particle hit rate from 7 MHz at 1.7 GeV/c to even 12 MHz at 0.69 GeV/c. The hit rates on the second tracking station (C2) were about an order of magnitude smaller, i.e. 800 kHz and 2 MHz, respectively.

The mutual correlation of amplitude and timing measurements in the tracking stations allowed to significantly reduce fake hit combinations and to identify individual pion tracks. The efficiencies of particle detection and track identification were determined for each LVL1 triggered event by various requirements on timing, positions, and pulse heights in both tracking stations. The observed detection efficiencies were $\epsilon = 92.5\%$ at 7 MHz for the upstream tracking station (C1) and $\epsilon = 93.2\%$ at 800 kHz for the downstream detector (C2). The resulting track identification efficiency was $\epsilon_{tr} = 87.0\%$. In the second run, in which the amplitude information of the upstream detector was not available, a significant increase in noise level and average multiplicities of three hits per event led to ambiguities in the impact localisation and hence to an efficiency decrease to $\epsilon = 86.5\%$ at about 12 MHz. For the respective run the detection efficiency of the C2 detector was $\epsilon = 90.2\%$ at 2 MHz hit rate and a resulting track finding efficiency 78.4%.

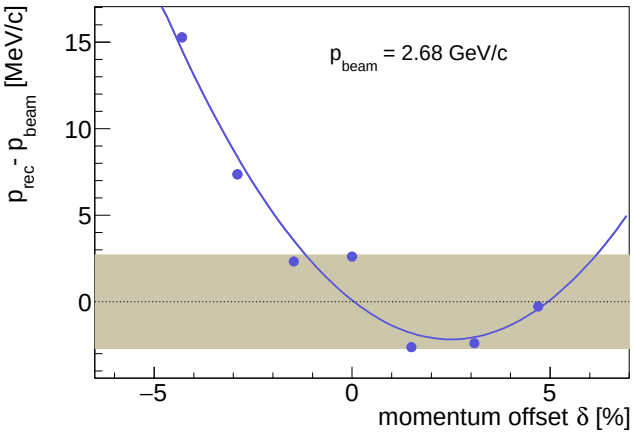

Fig. 16. (Color online) Absolute error on proton momenta (p_{rec} - p_{beam}) for seven different spectrometer beam line settings. Statistical errors are negligible. The error band represents the magnitude of systematic errors due to uncontrolled primary beam positions on the production target. The curve is the result of a parabolic fit.

4.2 Beam Optics Calibration

In the beam line calibration run, a proton beam ($p_{beam} = 2.68$ GeV/c) was focussed to the position of the primary production target. Incident beam positions and angles were varied up to $\Delta x_0 = \pm 1.4$ mm, $\Delta\theta_0 = \pm 2.2$ mrad in horizontal and $\Delta y_0 = \pm 0.7$ mm, $\Delta\phi_0 = \pm 7$ mrad in vertical directions. With the production target removed, monochromatic protons were then directed for various $B\rho$ (p_{ref}) settings of the beam line to the HADES target point. This procedure is equivalent to a variation of the primary beam momentum by the accelerator at constant reference $B\rho$ value [1].

The spectrometric beam line settings covered a momentum offset range $-4.3\% \leq \delta \leq +4.7\%$ (see equ. 2.2). The measured impact positions on the silicon detectors were then used to calculate reconstructed momentum values (p_{rec}). The most probable values of the distributions are shown in figure 16. The data points can be fitted by a parabola whose coefficients reflect the slight difference between the real and theoretical T16 and T166 coefficients. The important dispersion term T_{16}^{C1} at the first detector position was found to be only 3% lower than the

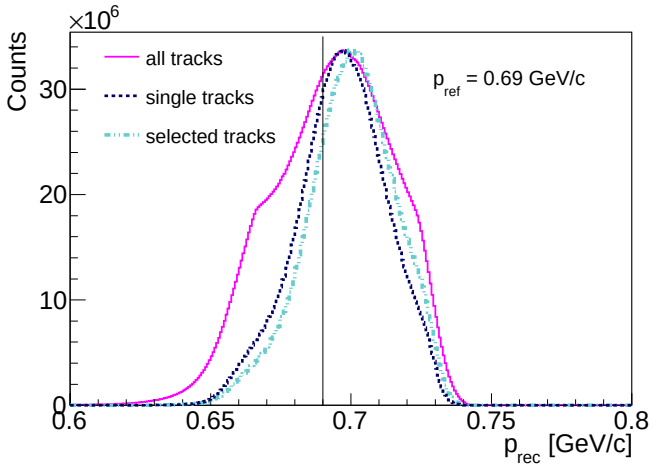

Fig. 17. (Color online) Reconstructed momentum distributions for tracks from all hit combinations (purple), for single hit tracks (dark blue), and for selected tracks (light blue) at a central beam of 0.69 GeV/c. The curves are normalized to same peak maximum values.

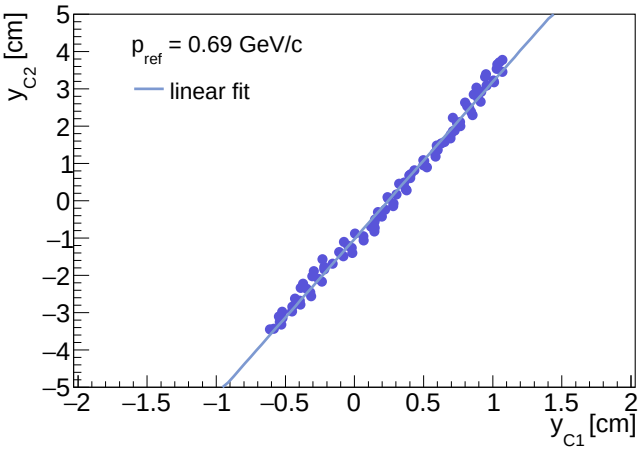

Fig. 18. (Color online) Correlation of y-positions in both detectors at $p_{ref} = 0.69$ GeV/c.

anticipated value emerging from the transport modelling. Other coefficients which could not be calibrated do not contribute significantly to the momentum resolution. The deviations are related to the different values of the dispersion coefficients and are not related to the resolution. The resolution is reflected in the width of the reconstructed momentum distributions at a given reference momentum. But, at 2.7 GeV/c, it is dominated by the horizontal width of the primary beam. The multiple scattering is much smaller than for pions, even at 1.7 GeV/c. Hence, these results can not be extrapolated.

An attempt was also made to determine the linear and angular magnification coefficients ($T_{11}, T_{12}, T_{33}, T_{34}$) by varying the position and angle of the incoming beam in the horizontal and vertical planes. Due to the lack of primary beam detectors and the sensitivity to small beam position fluctuations, these coefficients could not be determined accurately. However, significant deviations from the theoretical transport coefficients were observed. This is the case for example for the angular magnification term at the second detector position (T_{12}) which is found a factor about 2.5 smaller than predicted. Such deviations might affect e.g. the transmission of the pion beam line.

4.3 Momentum Reconstruction and Selection

The pion momenta were reconstructed using the measured track coordinates and applying the simulated transport coefficients. As an example, figure 17 depicts the distribution of reconstructed pion momenta for a central beam momentum of 0.690 GeV/c. The effect of multiple hits due to noise and high beam load in the first and second tracking station becomes visible, if they were not suppressed individually by the mutual timing and amplitude correlation in each detector. The general shift of the observed transmission maxima (p_{Mt}) to $p_{Mt} = 0.698$ GeV/c reflects a displacement of the hit distribution maxima also at the C1 detector in the dispersion plane. Corresponding shifts of $\simeq 1\%$ have been observed for all low momentum settings ($p_{ref} < 0.9$ GeV/c) and hint to a systematic discrepancy of nominal and effective reference momenta at the detector center positions. This discrepancy can not be explained by the energy loss in the tracking detectors, which stays below 1 MeV. It is also far too large to be explained by a systematic horizontal shift of the primary beam impact on the production target and may be attributed to a bad modeling of the magnetic fields in the dipoles due to remanence effects. Shifts of the primary beam in the vertical position can also affect the transmission of the beam line (see figure 6), resulting in a shift of the most probable pion beam momentum with respect to the reference value.

Prior to an event by event analysis a proper momentum value had to be determined from all available detector hits. This determination has been done to first order by localisation of the intensity maxima in C1 and C2 for well defined single hit tracks. Fake track suppression for multi hit events was achieved by requiring strict correlations also of y-positions in both tracking stations. For the second run, additional criteria became necessary, due to the missing amplitude information from C1 with resulting track ambiguities. The observed pattern depicted in figure 18 for well defined single tracks with precise determination of the transmission maximum exhibit the expected linear correlation. Averaged over the whole momentum acceptance the correlated y-positions follow the relation

$$y_{C2} = (4.2 \pm 0.3) \cdot y_{C1} - 1 \qquad (2)$$

with an effective slope parameter in reasonable agreement with the ratio of the first order transport coefficient T_{33}^{C2} / $T_{33}^{C1} = 3.76$ (see appendix 1). The offset points to the beam effects mentioned above.

In this way, the intensity distributions of single track events could well be reproduced also for multi track events.

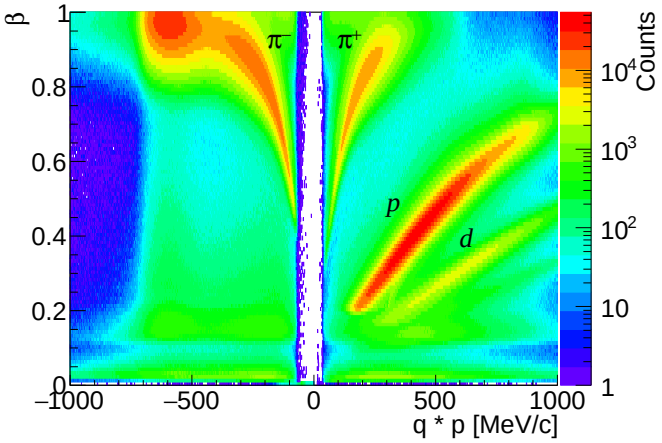

Fig. 19. Particle velocity β as a function of momentum after PID selection with spectrometer detectors for $p_{ref} = 0.69$ GeV/c.

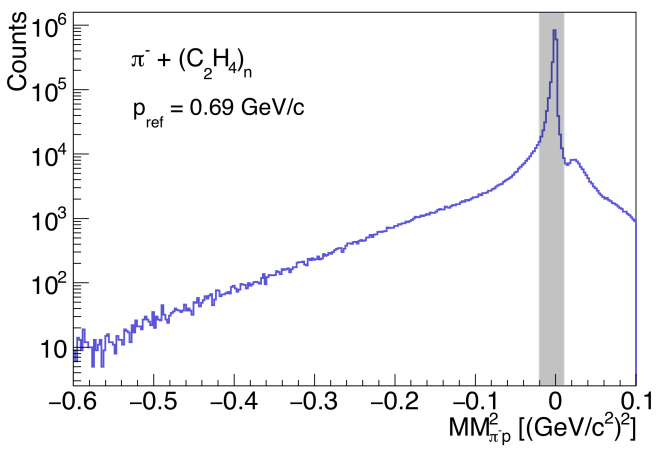

Fig. 20. Squared missing mass distribution for coplanar pions and protons detected in HADES.

The corresponding distribution of selected tracks is shown in figure 17. A small and negligible additional shift of about +2 MeV/c with respect to the nominal value is observed.

4.4 Elastic Scattering of Pions

The elastic scattering process off hydrogen nuclei in the compound PolyEthylene target (PE, $(C_2H_4)_n$) has been used to verify the reconstruction of the incident pion momenta. In the spectrometer data set, particle identification (PID) was performed utilizing time of flight measurement with the target T_0 and META detectors and momentum determination with the MDC tracking system in the HADES toroidal field. As an example, figure 19 shows the recorded velocity distributions as a function of particle momentum for the beam line setting corresponding to $p_{ref} = 0.69$ GeV/c.

The invariant mass $M_{\pi p}$ of elastic πp pairs measured with the HADES detectors is equal to the center of mass energy $\sqrt{s}$ available in the scattering process and hence provides an independent determination of the incomimng pion projectile momentum. Selecting exclusively events with track multiplicty two in the spectrometer and requiring coplanarity $175^\circ < \mid \varphi_{\pi^-} - \varphi_p \mid < 185^\circ$ for the particle trajectories allowed to construct the squared missing mass distribution ($MM^2_{\pi^- p}$) depicted in figure 20. The distinct peak at $MM^2_{\pi^- p} \approx 0$ $(GeV/c^2)^2$ identifies the elastic channel, while the tails originate from scattering off protons in the carbon nuclei and from inelastic processes. Inside the window -0.02 $(GeV/c^2)^2 < MM^2_{\pi p} < 0.01$ $(GeV/c^2)^2$ the contamination from non elastic scattering is expected to be on a 0.1 percent level.

For events inside the window, the $\pi^- p$ invariant mass distribution shown in figure 21 is compared to the distribution of the CMS energy for each event as deduced from the pion tracker information. As observed in figure 17, the CMS energy is higher than the value calculated with the reference momentum.

The $\pi^- p$ pair spectrum reconstructed with HADES (green curve) includes additional pion and proton momentum corrections originating partly from a systematic recalibration of HADES magnetic field values (of order $6 \cdot 10^{-3}$) and energy loss in beam tube, RICH radiator and target materials. The resulting curve exhibits a mean value of $M_{\pi p} = 1487\,MeV/c^2$ and a relative width of $\sigma(M_{\pi p}) \simeq 33$ MeV. A slightly higher mean value ($\sqrt{s} = 1496$ MeV/c^2, $\delta = +0.47\%$) of the $\sqrt{s}$ distribution is observed for the curve calculated from the reconstructed pion beam momenta. The width of this distribution is more than a factor 2 smaller ($\sigma(\sqrt{s}) \simeq 18$ MeV), equivalent to 1.7% on pion momentum, to be compared to the value of about 1% expected from the simulation of the beam line. This sizeable difference is probably due to the values of the vertical transport coefficients, which could not be measured and have a small effect on the momentum resolution, but a large effect on the transmission. Additionaly, possible misalignments and different sizes of magnetic elements or beam pipes have to be taken into account. It has to be noted that both distributions have been extracted for a short beam period with stable beam conditions, only.

Systematic discrepancies between invariant mass and center of mass energy of about $8 - 12$ MeV are observed for all beam line settings with $p_{ref} < 0.9$ GeV/c. In this paragraph, we discuss the possible origins of this discrepancy, i.e. energy loss effects, shifts of the beam positions in either horizontal or vertical direction, adjustments of the dipoles and remanence effects. Energy loss values obtained with GEANT4 simulations as well as tabulated in the NIST data base (GEANT4: 5.0 MeV/c ([67]) / NIST: 5.06 MeV/c ([68])) cannot explain this discrepancy itself assuming an average pion path length inside the target of $< l_{path} >= \frac{1}{2} \cdot l_{Target}$.

The discrepancy may be due to the following reasons:

– Shift of the primary beam in the horizontal direction: This induces an offset of 0.2%/mm in the momentum

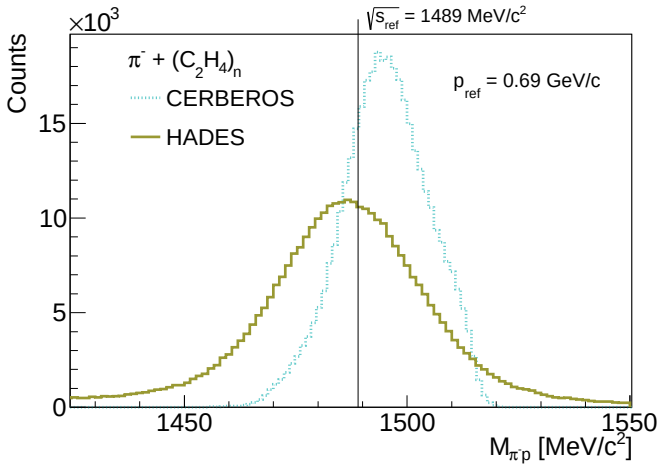

Fig. 21. (Color online) Energy ($\sqrt{s}$) distributions obtained for elastically scattered pion-proton pairs (green) and from pion beam momenta (light blue) assuming a nominal central beam momentum of 0.69 GeV/c.

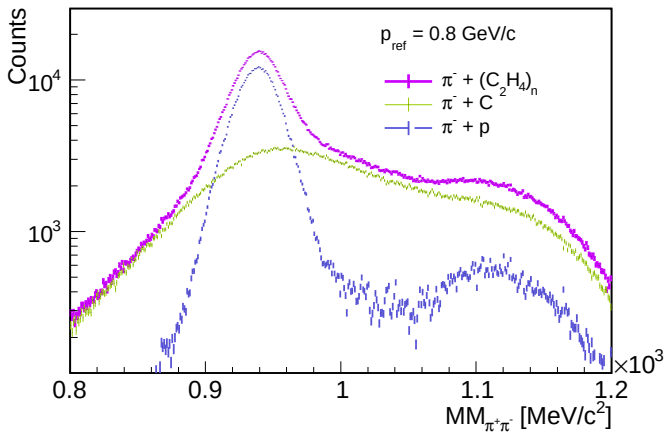

Fig. 22. Two-pion misssing mass distributions for pion beams accepted in the 800 MeV/c setting and impinging on the PE (purple) and C (green) target. The distribution for reactions on protons (blue) is obtained after normalisation and subtraction. Reaction channels with additional pions show up at higher missing masses.

reconstructed by CERBEROS, while the acceptance is almost not changed and therefore the mean center of mass energy reconstructed with spectrometer detectors is not affected.
- Shift of the primary beam in the vertical direction: This distorts the acceptance, with no significant error on the reconstructed pion momentum. This effect does not affect the relative spectra measured using either HADES or pion tracker information.
- Alignment of the beam line: The currents in the two dipoles had to be slightly adjusted to maximize the number of pions hitting the target, which in turn changed the transmission curve. However, the effect on the center of mass energy determination is estimated to be less than 1 MeV.
- Remanence effects: A possible error in the relation between the current in the magnets and the integrated magnetic field may induce a systematic shift of the reference momentum, and correspondingly of the invariant mass spectrum measured with HADES which is independent of the pion beam momentum. This interpretation is corroborated by the absence of a shift in the 1.7 GeV/c data set.

The offset observed on the reconstructed momentum using the pion tracker has finally been corrected for in the subsequent data analysis on a file by file basis.

While the nominal pion momenta had been calibrated before by elasting scattering on protons (see above), a respective verification was not possible for pion induced reactions on nuclear targets. Hence, the observed average corrections of $\simeq 1.5\%$ have been adopted as general uncertainties for these studies. For high resolution studies of exclusive reaction channels in the future, improved primary beam position monitoring and increased magnet stability seem to be mandatory.

4.5 Exclusive Two Pion Production Channels

The study of exclusive reaction channels in pion induced collisions with free protons are a central part of the forthcoming physics programme. In this commisioning campaign, we have studied two examples of pion production channels

$$\pi^- + p \rightarrow \pi^- + \pi^+ + n$$

and

$$\pi^- + p \rightarrow \pi^- + \pi^0 + p$$

.

Using these reactions, resolution effects related to the momentum reconstruction can be studied. Both final states have been identified on an event by event basis applying a PID selection similar to the $\pi^- + p \rightarrow \pi^- + p$ case in order to perform a partial wave analysis to determine corresponding baryon resonance amplitudes. The analysis has been performed for all four beam line settings corresponding to p_{ref} = 656, 690, 748 and 800 MeV/c and both reaction targets PolyEthylene (PE) and Carbon (C).

As an example, figure 22 depicts the missing mass distributions of two opposite charge pions measured for reactions on the PE and Carbon targets in the 800 MeV/c setting. Besides the distinct peak at the neutron mass value the maximum at higher missing masses resembles channels with additional pion production. After proper normalisation of both distributions to the same number of pion beam particles registered on the target T_0 detector and taking into account the different carbon atom densities, the resulting difference shows the reaction on hydrogen nuclei contained in the PE compound target. The respective distribution in the neutron mass region is confronted in figure 23 to two possible assumptions of input values for the incoming pion beam momentum: the most

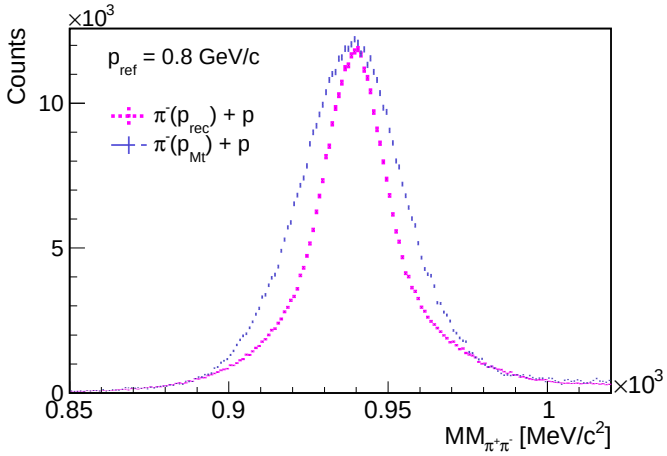

Fig. 23. Two-pion misssing mass distributions around the neutron pole for pion beams accepted in the 800 MeV/c setting reacting with hydrogen nuclei. The two curves are obtained for incident pion momenta assumed to be fixed (p_{Mt}, blue) and reconstructed with CERBEROS beam detectors (p_{rec}, pink).

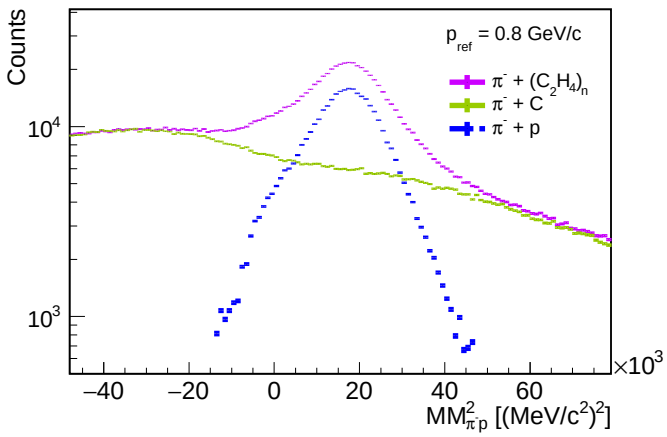

Fig. 24. Squared misssing mass distributions of pion-proton pairs measured for PE (purple) and C (green) targets and pion beams accepted in the 800 MeV/c setting. Contributions from elastic scattering are suppressed by kinematical cuts.

probable one fixed by the maximum transmission in the tracker spectrum (blue) and the one reconstructed event-by event (pink) with the beam tracking system. The peak position corresponds to the mass of the missing neutron (939.6 MeV/c^2) and shows a significantly better missing mass resolution for the reconstructed beam momentum ($\sigma = 1.04\%$) as compared to the fixed beam momentum hypothesis ($\sigma = 1.68\%$). Respective distributions for the 656 MeV/c setting give resolutions $\sigma = 0.83\%$ for the reconstructed and $\sigma = 1.4\%$ for the fixed mean momentum, respectively.

For the $\pi^- + p \to \pi^- + \pi^0 + p$ reaction channel, the strong $\pi^- p$ pair background originating from elastic scattering had to be discriminated via respective conditions on the kinematics. As an example, the resulting squared missing mass distribution shown in figure 22 for the 800 MeV/c setting exhibits a peak at $(\mathrm{MM}_{\pi p})^2 \simeq 17700 \simeq (133\ (\mathrm{MeV/c^2}))^2$ which is in very good agreement with the squared mass of the missing neutral pion. The yields at lower and higher squared masses stem predominantly from inelastic reactions on carbon nuclei. Proper normalisation and background subtraction allow to construct the squared missing mass distribution of the missing pion for the two assumptions on the input beam momentum (see figure 25). Again, the resolution for the beam momenta individually reconstructed by CERBEROS ($\sigma = 29\%$) is better than for the assumption of a fixed mean value ($\sigma = 39\%$), albeit on the expense of reduced efficiency (see paragraph 4.1).

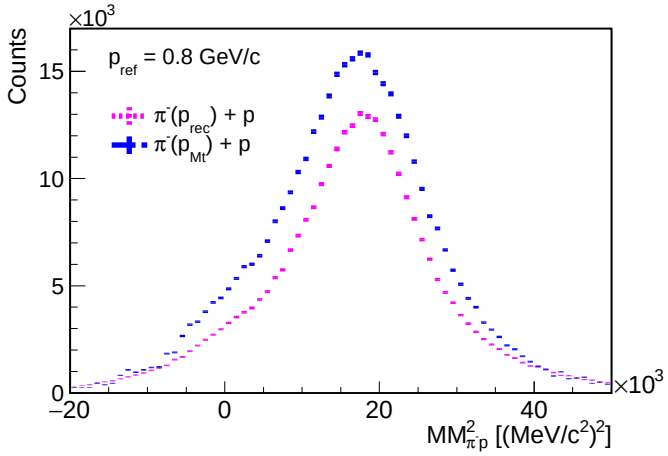

Fig. 25. Squared misssing mass distributions of pion-proton pairs around the missing π^0 mass after background subraction and for incident pion momenta assumed to be fixed (p_{Mt}, blue) or reconstructed event by event with CERBEROS beam detectors (p_{rec}, pink).

In summary, the CERBEROS beam tracking system improves significantly the reconstruction of exclusive reaction channels with single and multi pion final states and is mandatory for systematic studies of respective excitation functions.

5 Summary and Outlook

5.1 Summary

We have presented a secondary beam facility for the study of pion induced nuclear reactions with HADES at GSI, Darmstadt. Adapted to the SIS18 energy regime the facility can deliver in the future pions with momenta in the range $p_{\pi^-} = 0.4 - 2.0$ GeV/c and usable instantaneous beam currents close to $\simeq 10^6\ \pi^-/\mathrm{s}$ in a $\simeq 3$ second synchrotron cycle. We have developed and successfully operated a system for beam momentum reconstruction on the subpercent level at $\simeq 10^6 - 10^7\ \mathrm{s}^{-1}$ particle rates.

The facility is composed of a production target, a series of ion optical elements to guide the broad secondary pion beam to HADES, and two position sensitive in-beam

silicon detectors for pion momentum reconstruction. Detector signal readout is performed with the self-triggering n-XYTER chip with data output integrated into and synchronized with the TRB3-NET based HADES data acquisition system. Detailed TRANSPORT code studies have been performed to determine the optical properties of the beam line up to second order. Extensive Monte Carlo simulation studies allowed to optimize the position of the beam tracking detectors and of some quadrupoles. A dedicated algorithm to reconstruct the pion momentum was developed.

The system has been successfully operated in three experimental runs. Measurements with proton beams demonstrate that individual beam particle momenta can be reconstructed with a resolution of $\simeq 0.3\%$ (σ). In two further commissioning campaigns secondary pions were directed to HADES targets (C, W, $CH_2)_n$) in different $B\rho$ settings corresponding to central beam momenta p = 0.69 − 0.8 GeV/c and p = 1.7 GeV/c. The in-beam track and momentum reconstruction verified distibutions and resolutions as expected from the simulations.

The in-beam momentum reconstruction was verified independently by the analysis of elastic π^-+p scattering reactions extracted from spectrometer data of the π^- + $(C_2H_4)_n$ runs. A corresponding analysis of the reaction $\pi^- + p \rightarrow \pi^- + \pi^+ + n$ and $\pi^- + p \rightarrow \pi^- + \pi^0 + p$ demonstrates that the missing mass resolutions can be improved by $\simeq 40\%$ if the pion momentum reconstructed via the in-beam detectors is included in the analysis. These results show the feasibility of experimental pion nucleon interactions studies even in exclusive reaction channels.

5.2 Outlook

The availabilty of secondary pion beams and the versatile HADES detector opens up a new era for future precision measurements of pion induced reactions on protons and heavy nuclei in the 1 GeV energy regime. Currently, dedicated efforts have been started by the accelerator group to allow for routine and long-time operation of the SIS18 synchrotron at its space charge limit. This will provide maximum primary and secondary beam intensities at reasonable emittances, spill structures and position stabilities mandatory for extended measurement campaigns. Forthcoming improvements for the in-beam detector readout including the time resolution of the silicon detectors and the amplitude measurement also in the first station will substantially enhance the track reconstruction efficiency and background discrimination.

The planned experiments cover a broad physics programme including measurements of baryonic resonances and their coupling to vector mesons with successive decay into dilepton pairs as well as the study of vector and strange mesons inside nuclei. It also enables baryon spectroscopy studies in various meson production channels including kaons and, in the near future, also neutral mesons (π^0, η) thanks to the addition of an electromagnetic calorimeter to the HADES detector. The ongoing construction of a straw tube detection system at forward angles will also enlarge the present acceptance for charged particles. The new experimental access to high interaction rates, precise beam momentum selection, large spectrometer acceptance and state-of-the-art data acquisition will allow to collect data sets with event statistics for inclusive and exclusive reaction channels far beyond present values. It is widely acknowledged that progress in the field of baryon spectroscopy is hampered by the lack of data from pion-induced experiments. This new facility will help to complement the data coming from circularly- and linearly-polarized photon beams at ELSA, MAMI, JLab, LEPS as well as from electron beams at CLAS (soon CLAS12 also) and may act as a precursor for other projects of meson beam facilities [4]. Apart from a better understanding of elementary pion nucleon interactions, the new facility will also significantly contribute to the general question of how hadrons propagate in cold baryonic matter and nuclear fireballs as well as their possible connection to the quest of chiral symmetry restoration.

Acknowledgements

The HADES collaboration gratefully acknowledges the support given by the following institutions and agencies: SIP JUC Cracow6, 2013/10/M/ST2/00042 (Poland); TU Darmstadt, VH-NG-823, (Germany); GU Frankfurt, BMBF:05P15RFFCA, HIC for FAIR, ExtreMe Matter Institute EMMI (Germany); TU München, DFG EClust153, BMBF:05P15WOFCA, DFG FAB898/2-1, MLL Garching,(Germany); JLU Giessen, BMBF:05P12RGGHM (Germany); CNRS/IN2P3, IPN Orsay (France); NPI CAS Rez, GACR:13-06759S, MSMT:LM2015049,(Czech Republic).

References

1. J. Diaz *et al.*, Nucl. Instrum. Meth. A **478** (2002) 511–526.
2. J. Wirth, L. Fabbietti, R. Lalik, L. Maier, A. Scordo, Nucl. Instrum. Meth. A **824** (2016) 243–244.
3. G. Agakishiev *et al.*, Eur. Phys. J. A **41** (2009) 243–277.
4. W. J. Briscoe, M. Doering, H. Haberzettl, D. M. Manley, M. Naruki, I. I. Strakovsky, E. S. Swanson, Eur. Phys. J. A **51** (10) (2015) 129.
5. A. V. Anisovich, R. Beck, E. Klempt, V. A. Nikonov, A. V. Sarantsev, U. Thoma, Eur. Phys. J. A **48** (2012) 15.
6. N.N, SAID data base http://aea.web.psi.ch/Urs_Rohrer/MyWeb/trans.htm.
7. P. Strzempek, Nucl. Instrum. Meth. A **824** (2016) 359–361.
8. M. Doring, C. Hanhart, F. Huang, S. Krewald, U. G. Meissner, Nucl. Phys. A **829** (2009) 170–209.
9. M. Doring, C. Hanhart, F. Huang, S. Krewald, U. G. Meissner, Phys. Lett. B **681** (2009) 26–31.
10. D. J. Candlin *et al.*, Nucl. Phys. B **238** (1984) 477–491.
11. V. Shklyar, H. Lenske, U. Mosel, Phys. Rev. C **72** (2005) 015210.
12. S. Abd El-Samad *et al.*, Eur. Phys. J. A **49** (2013) 41.
13. H. Machner, J. Haidenbauer, F. Hinterberger, A. Magiera, J. A. Niskanen, J. Ritman, R. Siudak, Nucl. Phys. A **901** (2013) 65–88.
14. S. Jowzaee *et al.*, Eur. Phys. J. A **52** (1) (2016) 7.

15. E. Oset, A. Ramos, Eur. Phys. J. A **44** (2010) 445–454.
16. Y. S. Golubeva, L. A. Kondratyuk, W. Cassing, Nucl. Phys. A **625** (1997) 832–854.
17. M. Effenberger, E. L. Bratkovskaya, W. Cassing, U. Mosel, Phys. Rev. C **60** (1999) 027601.
18. G. Agakishiev *et al.*, Phys. Lett. B **715** (2012) 304–309.
19. M. Naruki *et al.*, Phys. Rev. Lett. **96** (2006) 092301.
20. W. Schon, H. Bokemeyer, W. Konig, V. Metag, Acta Phys. Polon. B **27** (1996) 2959–2963.
21. F. Sakuma *et al.*, Phys. Rev. Lett. **98** (2007) 152302.
22. M. Benabderrahmane *et al.*, Phys. Rev. Lett. **102** (2009) 182501.
23. V. Koptev *et al.*, Phys. Rev. Lett. **87** (2001) 022301.
24. O. Vzquez Doce *et al.*, Phys. Lett. B **758** (2016) 134–139.
25. G. Agakishiev *et al.*, Phys. Rev. C **92** (2) (2015) 024903.
26. G. Agakishiev *et al.*, Phys. Lett. B **742** (2015) 242–248.
27. G. Agakishiev *et al.*, Phys. Rev. C **90** (2014) 015202.
28. G. Agakishiev *et al.*, Phys. Rev. C **90** (2014) 054906.
29. G. Agakishiev *et al.*, Eur. Phys. J. A **50** (2014) 81.
30. M. Hartmann, Y. Kiselev, A. Polyanskiy, E. Y. Paryev, M. Buscher *et al.*, Phys. Rev. C **85** (2012) 035206.
31. R. Muto *et al.*, Phys. Rev. Lett. **98** (2007) 042501.
32. D. B. Kaplan, A. E. Nelson, Phys. Lett. B **175** (1986) 57–63.
33. J. Schaffner, J. Bondorf, I. N. Mishustin, Nucl. Phys. A **625** (1997) 325–346.
34. W. Cassing, E. L. Bratkovskaya, U. Mosel, S. Teis, A. Sibirtsev, Nucl. Phys. A **614** (1997) 415–432.
35. D. Cabrera, L. Tolos, J. Aichelin, E. bratkovskaya, J. Phys. Conf. Ser. **668** (1) (2016) 012048.
36. D. Cabrera, L. Roca, E. Oset, H. Toki, M. Vicente Vacas, Nucl. Phys. A **733** (2004) 130–141.
37. C. Dover, J. Huefner, R. H. Lemmer, Annals Phys. **66** (1971) 248–292.
38. T. Ishikawa *et al.*, Phys. Lett. B **608** (2005) 215–222.
39. P. Muhlich, and U. Mosel, Nucl. Phys. A **765** (2006) 188–196.
40. A. Polyanskiy *et al.*, Phys. Lett. B **695** (2011) 74–77.
41. E. Friedman, A. Gal, Nucl. Phys. A **899** (2013) 60–75.
42. E. Friedman, A. Gal, Nucl. Phys. A **959** (2017) 66–82.
43. Yu. T. Kiselev *et al.*, Phys. Rev. C **92** (2015) 065201.
44. M. F. M. Lutz, B. Friman, M. Soyeur, Nucl. Phys. A **713** (2003) 97–118.
45. A. I. Titov, B. Kämpfer, Eur. Phys. J. A **12** (2001) 217–229.
46. B. Friman, M. F. M. Lutz, G. Wolf, Nucl. Phys. A **654** (1) (1999) 615c–618c.
47. M. F. M. Lutz, G. Wolf, B. Friman, Nucl. Phys. A **706** (2002) 431–496, [Erratum: Nucl. Phys.A765,495(2006)].
48. A. Faessler, C. Fuchs, M. I. Krivoruchenko, B. V. Martemyanov, J. Phys. G **29** (2003) 603–624.
49. E. Speranza, M. Zetenyi, B. Friman, Phys. Lett. B **764** (2017) 282–288.
50. U. Rohrer, PSI Graphic Transport Framework by U. Rohrer based on a CERN-SLAC-FERMILAB version by K.L. Brown et al (2007) http://aea.web.psi.ch/Urs_Rohrer/MyWeb/trans.htm.
51. I. Frohlich *et al.*, PoS ACAT2007 (2007) 076.
52. G. Agakishiev *et al.*, Eur. Phys. J. A **40** (2009) 45–59.
53. C. Theisen *et al.*, Nucl. Instrum. Meth. A **747** (2014) 69–80.
54. M. Friedl, Ph.D. thesis, Vienna University of Technology (2001).
55. J. Siebenson, Ph.D. thesis, TU München (2013).
56. N. Abel, CBM Progress Report 2008.
57. G. Lindstrom, M. Moll, E. Fretwurst, Nucl. Instrum. Meth. A **426** (1999) 1–15.
58. G. Lindstrom, Nucl. Instrum. Meth. A **512** (2003) 30–43.
59. G. Lutz, *Semiconductor radiation detectors device physics*, (Springer, Berlin New York), 2007.
60. T. Kohriki, T. Kondo, H. Iwasaki, S. Terada, Y. Unno, T. Ohsugi, IEEE Trans. Nucl. Sci. **43** (1996) 1200–1202.
61. A. S. Brogna, S. Buzzetti, W. Dabrowski, T. Fiutowski, B. Gebauer, M. Klein, C. J. Schmidt, H. K. Soltveit, R. Szczygiel, U. Trunk, Nucl. Instrum. Meth. A **568** (2006) 301–308.
62. J. Michel *et al.*, JINST **6** (2011) C12056.
63. A. Neiser *et al.*, JINST **8** (2013) C12043.
64. J. Pietraszko, L. Fabbietti, W. Koenig, Nucl. Instrum. Meth. A **618** (2010) 121–123.
65. F. Anghinolfi, P. Jarron, F. Krummenacher, E. Usenko, M. C. S. Williams, IEEE Trans. Nucl. Sci. **51** (2004) 1974–1978.
66. C. Ugur *et al.*, IEEE Nordic Mediterranean Workshop on Time-to-Digital Converters (2013).
67. S. Agostinelli *et al.*, Nucl. Instrum. Meth. A **506** (2003) 250–303.
68. National Institute of Standards and Technology. http://physics.nist.gov/PhysRefData/Star/Text/PSTAR-t.html.

6 Appendix: Beam Line Optics

6.1 Transport Coefficients

The first and second order transport coefficients were obtained in calculations with the TRANSPORT code [50]. The values of the most significant coefficients used for the reconstruction of pion momentum and impact position on the HADES target (see paragraph 2.4) are listed below.

Table 3. Numerical values of the transport coefficients in the horizontal plane at the two detector positions C1 and C2.

Coefficient	Detector C1	Detector C2
T_{11}^{det} [cm/cm]	-1.747	-9.634×10^{-1}
T_{12}^{det} [cm/mrad]	-3.919×10^{-2}	-4.745×10^{-1}
T_{14}^{det} [cm/mrad]	-1.11×10^{-3}	6.000×10^{-5}
T_{16}^{det} [cm/%]	-8.1235×10^{-1}	-3.413×10^{-2}
T_{116}^{det} [cm/cm/%]	1.519×10^{-1}	-1.86×10^{-1}
T_{126}^{det} [cm/mrad/%]	3.095×10^{-2}	-3.080×10^{-2}
T_{146}^{det} [cm/mrad/%]	-3.049×10^{-4}	8.834×10^{-4}
T_{166}^{det} [cm/%^{2}]	5.611×10^{-3}	-2.265×10^{-2}

Table 4. Numerical values of the transport coefficients in the vertical plane at the two detector positions.

Coefficient	Detector C1	Detector C2
T_{32}^{det} [cm/mrad]	-1.312×10^{-2}	-6.929×10^{-2}
T_{33}^{det} [cm/cm]	-1.828×10^{1}	-6.787×10^{1}
T_{34}^{det} [cm/mrad]	-2.98×10^{-3}	-8.382×10^{-2}
T_{36}^{det} [cm/%]	3.955×10^{-1}	1.424
T_{336}^{det} [cm/cm/%]	2.160×10^{-1}	8.774×10^{-1}
T_{346}^{det} [cm/mrad/%]	2.63×10^{-2}	9.678×10^{-2}
T_{366}^{det} [cm/%^{2}]	-3.661×10^{-3}	-1.531×10^{-2}

Table 5. Numerical values of the transport coefficients between the pion production target and the HADES target.

Coefficient	Value
T_{22}^{H} [mrad/mrad]	-0.57575
T_{23}^{H} [mrad/cm]	-1.1625
T_{26}^{H} [mrad/\$]	7.783×10^{-2}
T_{226}^{H} [mrad/mrad/%]	-4.209×10^{-2}
T_{246}^{H} [mrad/mrad/%]	1.718×10^{-3}
T_{266}^{H} [mrad/%^{2}]	2.538×10^{-2}
T_{42}^{H} [mrad/mrad]	2.658×10^{-1}
T_{43}^{H} [mrad/cm]	2.6323×10^{2}
T_{44}^{H} [mrad/mrad]	3.2118×10^{-1}
T_{46}^{H} [mrad/%]	-5.581
T_{426}^{H} [mrad/mrad/%]	-3.304×10^{-3}
T_{436}^{H} [mrad/cm/%]	-8.383
T_{446}^{H} [mrad/mrad/%]	-3.817×10^{-1}
T_{466}^{H} [mrad/%^{2}]	1.623×10^{-1}

6.2 Solving the Equations

Since one cannot extract five unknown variables out of a set of four equations (Eq.1), one assumes that the particles are emitted at $x_0 = 0$. In this case, the corresponding terms $T_{11}x_0$ and $T_{116}x_0\delta$ drop out and the system of four equations reads:

$$\begin{cases} X^{\mathrm{C1}} = T_{12}^{\mathrm{C1}} \cdot \theta_0 + T_{14}^{\mathrm{C1}} \cdot \varphi_0 + T_{16}^{\mathrm{C1}} \cdot \delta \\ \quad + T_{126}^{\mathrm{C1}} \cdot \theta_0\delta + T_{146}^{\mathrm{C1}} \cdot \varphi_0\delta + T_{166}^{\mathrm{C1}} \cdot \delta^2, \\ X^{\mathrm{C2}} = T_{12}^{\mathrm{C2}} \cdot \theta_0 + T_{14}^{\mathrm{C2}} \cdot \varphi_0 + T_{16}^{\mathrm{C2}} \cdot \delta \\ \quad + T_{126}^{\mathrm{C2}} \cdot \theta_0\delta + T_{146}^{\mathrm{C2}} \cdot \varphi_0\delta + T_{166}^{\mathrm{C2}} \cdot \delta^2, \\ Y^{\mathrm{C1}} = T_{32}^{\mathrm{C1}} \cdot \theta_0 + T_{33}^{\mathrm{C1}} \cdot y_0 + T_{34}^{\mathrm{C1}} \cdot \varphi_0 \\ \quad + T_{36}^{\mathrm{C1}} \cdot \delta + T_{336}^{\mathrm{C1}} \cdot y_0\delta + T_{346}^{\mathrm{C1}} \cdot \varphi_0\delta \\ \quad + T_{366} \cdot \delta^2, \\ Y^{\mathrm{C2}} = T_{32}^{\mathrm{C2}} \cdot \theta_0 + T_{33}^{\mathrm{C2}} \cdot y_0 + T_{34}^{\mathrm{C2}} \cdot \varphi_0 \\ \quad + T_{36}^{\mathrm{C2}} \cdot \delta + T_{336}^{\mathrm{C2}} \cdot y_0\delta + T_{346}^{\mathrm{C2}} \cdot \varphi_0\delta \\ \quad + T_{366}^{\mathrm{C2}} \cdot \delta^2. \end{cases}$$

It contains twentysix transport coefficients obtained from beam transport calculations and four measured particle positions X^{C1}, Y^{C1}, X^{C2} and Y^{C2} on the two detectors. The parameters relating the measured horizontal (X^{C1} , X^{C2}) and vertical (Y^{C1}, Y^{C2}) detector positions are given in tables 3 and 4, respectively.

The remaining terms $T_{11}x_0$ and $T_{116}x_0\delta$ will contribute significantly to the momentum resolution, besides contributions from multiple scattering in detector C1 and achievable detector position resolutions at X^{C1}, X^{C2}, Y^{C1} and Y^{C2}.

To solve this set of equations, we neglect in the first iteration the terms $T_{14}\varphi_0$ and $T_{146}\varphi_0\delta$ that couple to the vertical variables. Consequently, the first two equations contains only the two variables θ_0 and δ and can then be solved independently. A third order equation in δ is then derived and reads

$$a_0 + a_1\delta + a_2\delta^2 + a_3\delta^3 = 0$$

with

$$\begin{aligned} a_0 &= X^{\mathrm{C2}}T_{12}^{\mathrm{C1}} - X^{\mathrm{C1}}T_{12}^{\mathrm{C2}}, \\ a_1 &= \left(X^{\mathrm{C2}}T_{126}^{\mathrm{C1}} - T_{12}^{\mathrm{C1}}T_{16}^{\mathrm{C2}}\right), \\ &\quad - \left(X^{\mathrm{C1}}T_{126}^{\mathrm{C2}} - T_{12}^{\mathrm{C2}}T_{16}^{\mathrm{C1}}\right), \\ a_2 &= \left(T_{16}^{\mathrm{C1}}T_{126}^{\mathrm{C2}} + T_{12}^{\mathrm{C2}}T_{166}^{\mathrm{C1}}\right), \\ &\quad - \left(T_{16}^{\mathrm{C2}}T_{126}^{\mathrm{C1}} + T_{12}^{\mathrm{C1}}T_{166}^{\mathrm{C2}}\right), \\ a_3 &= T_{126}^{\mathrm{C2}}T_{166}^{\mathrm{C1}} - T_{126}^{\mathrm{C1}}T_{166}^{\mathrm{C2}}. \end{aligned} \tag{3}$$

and is solved either analytically or numerically with a start value at $\delta = 6\%$. The θ_0 value can then be deduced. The values of θ_0 and δ are introduced in the last two equations, leading to the following linear system:

$$\begin{cases} \alpha y_0 + \beta\varphi_0 = \gamma, \\ \alpha' y_0 + \beta'\varphi_0 = \gamma'. \end{cases} \tag{4}$$

with

$$\begin{aligned}
\alpha &= T^{\mathrm{C1}}_{33} + T^{\mathrm{C1}}_{336} \cdot \delta, \\
\alpha' &= T^{\mathrm{C2}}_{33} + T^{\mathrm{C2}}_{336} \cdot \delta, \\
\beta &= T^{\mathrm{C1}}_{34} + T^{\mathrm{C1}}_{346} \cdot \delta, \\
\beta' &= T^{\mathrm{C2}}_{34} + T^{\mathrm{C2}}_{346} \cdot \delta, \\
\gamma &= Y^{\mathrm{C1}} - T^{\mathrm{C1}}_{32} \cdot \theta_0 - T^{\mathrm{C1}}_{36} \cdot \delta - T^{\mathrm{C1}}_{366} \cdot \delta^2, \\
\gamma' &= Y^{\mathrm{C2}} - T^{\mathrm{C2}}_{32} \cdot \theta_0 - T^{\mathrm{C2}}_{36} \cdot \delta - T^{\mathrm{C2}}_{366} \cdot \delta^2.
\end{aligned} \tag{5}$$

(6)

The solutions of this system are fed into the first 2 equations (the ones involving X^{C1} and X^{C2}) which is solved again for providing the final values for θ_0 and δ. The convergence is quite fast and one iteration is enough to keep residuals on δ much below the per mil level. A second iteration on the two last equations involving Y^{C1} and Y^{C2} provides then final values for φ_0 and y_0.

The relevant quantities for kinematical reconstruction of the events, p_x,p_y, and p_z at the HADES target point are derived from the values of θ_0, φ_0, and δ through the formula:

$$\begin{aligned}
p &= p_{spec}(1+\delta) \\
p_x &= \frac{p \tan(\theta_H)}{\sqrt{1+\tan^2(\theta_H)+\tan^2(\varphi_H)}}, \\
p_y &= \frac{p \tan(\varphi_H)}{\sqrt{1+\tan^2(\theta_H)+\tan^2(\varphi_H)}}, \\
p_z &= \frac{p}{\sqrt{1+\tan^2(\theta_H)+\tan^2(\varphi_H)}},
\end{aligned} \tag{7}$$

where θ_H and φ_H are obtained through the following relations (see 5 for the coefficients)

$$\begin{aligned}
\theta_H &= T^{\mathrm{H}}_{22} \cdot \theta_0 + T^{\mathrm{H}}_{23} \cdot y_0 + T^{\mathrm{H}}_{26} \cdot \delta \\
&\quad + T^{\mathrm{H}}_{226} \cdot \theta_0\delta + T^{\mathrm{H}}_{246} \cdot \varphi_0\delta + T^{\mathrm{H}}_{266} \cdot \delta^2, \\
\varphi_H &= T^{\mathrm{H}}_{42} \cdot \theta_0 + T^{\mathrm{H}}_{43} \cdot y_0 + T^{\mathrm{H}}_{44} \cdot \varphi_0 + T^{\mathrm{H}}_{46} \cdot \delta \\
&\quad + T^{\mathrm{H}}_{426} \cdot \theta_0\delta + T^{\mathrm{H}}_{436} \cdot y_0\delta + T^{\mathrm{H}}_{446} \cdot \varphi_0\delta + T^{\mathrm{H}}_{466} \cdot \delta^2.
\end{aligned}$$

6.3 Handling Coordinate Changes in Simulation

In the basic transport simulation of negative pions in the spectrometic line, the momentum offset δ of the particle's coordinate $\mathbf{X} = (x, \theta, y, \varphi, \delta)$ remains constant, and the only changes to the other components follow the second order transport equation Eq. (1). These equations allow to calculate the coordinates $\mathbf{X}_L$ of a particle at any point of distance L from the production target along the beam line, given its initial state at the production target $\mathbf{X}_0$.

However, if momentum or angle of a particle changes in-flight, as it can happen via multiple scattering (change in angle only) or for a pion via decay into a muon (change in δ, ϑ, and φ), the calculation of the new trajectory requires in principle new transport equations starting from the point where these changes have occurred. In the present case, we use a simpler treatment for such cases and proceed by first simulating the new particle coordinates $\mathbf{X}'_L = (x'_L = x_L, \theta'_L, y'_L = y_L, \varphi'_L, \delta'_L)$ and follow the kinematics of the process that produced the change. In the case of multiple scattering inside a detector, the change in θ and φ is computed by accounting for thickness and interaction length of the material. For pion decays, θ, φ and δ are calculated using two body decay kinematics with a uniform polar angle distribution for the muon in the pion rest frame and transforming the resulting momentum vector into beam line coordinates.

Once $\mathbf{X}'_L$ is known, we solve the equation

$$T_L \mathbf{X}'_0 = \mathbf{X}'_L \tag{8}$$

for $\mathbf{X}'_0$, the coordinates of a hypothetical particle at the production target, such that the application of Eq. (1) to $\mathbf{X}'_0$ using the transport matrix T_L to position L results in the modified coordinate $\mathbf{X}'_L$. There are multiple approaches for solving Eq. (8) for $\mathbf{X}'_0$. One possibility is to approximate the second order equation by a first order matrix multiplication, where only the second order terms dependent on δ are kept. This is possible because δ does not change in Eq. (8), and the second order effects of terms that do not have any dependence on δ is small. For our simulation we used an iterative approach, where Eq. (8) is minimized with the coordinates of $\mathbf{X}'_0$ as free parameters.

Once $\mathbf{X}'_0$ has been determined, the second order transport equations Eq. (1) are applied to $\mathbf{X}'_0$ for all acceptance check points downstream of the multiple scattering or decay position up to the next location where a coordinate change is necessary. This is repeated until all multiple scattering points and potential pion decay points have been treated.